Noname manuscript No.
(will be inserted by the editor)

Corrected trapezoidal rule for near-singular integrals in axi-symmetric Stokes flow

Monika Nitsche

Received: date / Accepted: date

Abstract The paper presents a method to evaluate near-singular boundary integrals in axi-symmetric interfacial Stokes flow for target points close to but not on the interface. The method consists of appoximating the integrand by a function with analytically available integral and numerically approximating the difference by a standard 4th order trapezoidal rule with uniform meshsize h. The resulting correction is applied to all points at distance d sufficiently close to the boundary. The maximum errors are reduced from order $O(h/d)$ to $O(h^m)$, where m depends on the number of terms in the approximating function. The paper presents all necessary details in the axi-symmetric Stokes case, implements specific $O(h^2)$, $O(h^3)$ and $O(h^4)$ versions, and shows that the analytically predicted convergence rates are attained for sample test cases. The method is applied to compute the evolution of double emulsions through a tapered nozzle and shown to resolve the unphysical tangling of interfaces that occurs with standard quadratures.

Keywords near-singular integrals · axi-symmetric Stokes flow · boundary integral method · interfacial flow

Statements and Declaration The author has no relevant financial or non-financial interests to disclose.

1 Introduction

Stokes equations model incompressible fluid flows in the limit of vanishing Reynolds number, and are the model of choice when length scales are on the order of micrometers. These are the scales of microfluidic devices, which have a large range of applications in areas such as biomedicine, microscale chemical production, drug delivery, food processing, inkjet printing and cosmetics. Understanding droplet motion in these devices is fundamental to the device design. One particular aspect

M. Nitsche
Department of Mathematics and Statistics
University of New Mexico
E-mail: nitsche@unm.edu

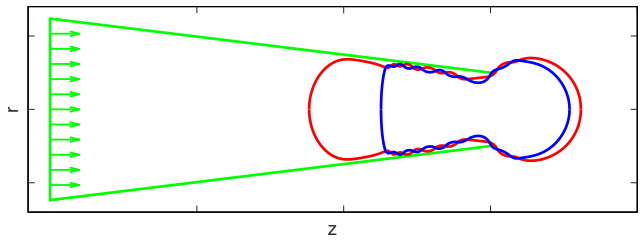

Fig. 1 Simulation of double emulsion (red and blue) flowing through a tapered nozzle (green), driven by a uniform flow in the back of the nozzle.

of interest is to develop a good understanding of droplet breakup [2]. The present work is focused on droplet motion in axi-symmetric geometries. It is motivated by an experiment performed by Chen *et. al*[10], who explored the breakup of double emulsions flowing through a tapered nozzle. The emulsions consist of a double droplet with an inner phase in the inner droplet, surrounded by a shell phase in the outer droplet, flowing in an outer phase, in this case water. The objective of the experiment was to determine in which parameter regime the droplets break, thus releasing the inner phase, and what the composition of droplets is after breakup. Due to the axi-symmetric geometry and the small length scales, this sample flow is well modeled by the axi-symmetric Stokes equations. The ultimate goal of the present work is to study the motion of such drops or double droplets through constrained geometries using numerical simulations.

Interfacial flows in Stokes flow are efficiently simulated using a boundary integral formulation (BIF) of the governing elliptic partial differential equations. The BIF enables us to accurately resolve the interface motion, accomodating moving boundaries of arbitrary shape, at low cost since the dimension of the interfaces is one lower than that of the fluid domain. The boundary integrals provide a representation of the fluid velocity at any target point $\mathbf{x}_0$. If $\mathbf{x}_0$ lies on an interface S, the integral over that interface is generally singular. If $\mathbf{x}_0$ lies far away from S, the integral over that interface is regular. In both cases, well established methods exist to accurately evaluate them. However, if $\mathbf{x}_0$ is not on S but close to it, at a small distance d, the integral is near-singular and standard quadratures are known to lose accuracy as $d \to 0$.

An example illustrating the consequence of inaccuracies is given in figure 1. The figure shows an instant during the motion of double droplets through a tapered nozzle in axi-symmetric Stokes flow, driven by a parallel flow at the back of the nozzle. In axi-symmetric geometry, all boundary integrals reduce to line integrals over curves in the symmetry z-r plane, where z is the axial and $r \geq 0$ the radial coordinate. The figure shows the nozzle (green), outer drop (red) and inner drop (blue) in the z-r plane, in addition to the symmetric image for $r < 0$. The fluid velocity at any point $\mathbf{x}_0$ is given by a sum of line integrals over all three curves. At the instant shown, the blue and red curves have tangled due to inaccuracies when the interfaces are close to each other. A short time later this particular simulation breaks down. In order to accurately resolve the drop motion, we need to apply a method to resolve the axi-symmetric boundary integrals in the near-singular case. The presentation and evaluation of such a method is the purpose of this paper.

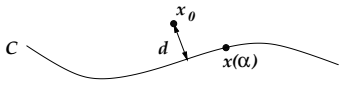

Fig. 2 Sketch showing curve C given by $\mathbf{x}(\alpha)$ with target point $\mathbf{x}_0$ at distance d from C.

Accurate evaluation of near-singular integrals has been the subject of extensive research, motivated by solutions to the Laplace, Helmholtz or Stokes equations. While plain adaptive quadrature is a possible approach, the numerical cost is high when $d \ll 1$. By now, several alternative methods have been developed. The most simple and accurate ones are based on complex variable representations in planar geometries [32,14,33,4,3]. However, the integrands in axi-symmetric geometry are not analytic and these methods cannot be applied here. Another accurate and well-understood approach that has been generalized to a range of kernels is the method of quadrature-by-expansion (QBX), in which the integrals are expanded about points in the interior of the fluid, at sufficient distance from the boundary that all integrals can be evaluated accurately [21,12,18–20,38,41]. Other approaches include matched asymptotics [9]; integrand regularization coupled with asymptotic approximations of the regularization error [5,11,44,6,45]; interpolation of integral values in the domain interior [48,37]; interpolation of the density on the boundary coupled with identities in Stokes flow that reduce the near-singularity [34]; and asymptotic approximations of the integrals [17]. Most of these methods have been applied in planar geometries, and several have been extended to 3D, although no particular results for axi-symmetric geometries exist. Here we apply a method most closely resembling corrected trapezoidal rules for singular integrals [40,39,26,27, 30,24,47,46]. The method was introduced in [28] and applied to planar potential and vortex sheet flow. The current version for axisymmetric Stokes flow may also be applicable to the types of problems addressed in [16,13].

The method. The goal is to evaluate line integrals of the form

$$\int_a^b \frac{F_{p/2}(\mathbf{x},\mathbf{x}_0)}{|\mathbf{x}-\mathbf{x}_0|^p}\,\omega(\alpha)\,d\alpha, \quad \int_a^b F_0(\mathbf{x},\mathbf{x}_0)\log|\mathbf{x}-\mathbf{x}_0|^2\,\omega(\alpha)\,d\alpha, \tag{1.1}$$

for any integer p. Here, F is a problem dependent kernel, assumed to be smooth. The variable $\mathbf{x} = \mathbf{x}(\alpha)$, $\alpha \in [a,b]$ is a parametrization of a curve C in the plane, $\omega(\alpha)$ is the density function, and $\mathbf{x}_0$ is a fixed target point not on C, but at a small distance d, as illustrated in figure 2. The curve $\mathbf{x}(\alpha)$ and density $\omega(\alpha)$ are also assumed to be sufficiently smooth, as required for the desired order of accuracy. In axi-symmetric Stokes flow the relevant cases are $p = 2,3,4,5,7,9$ and the logarithmic near-singularity, all of which appear in the governing boundary integrals.

The method was developed to be applicable for any kernel F. It is based on Taylor series approximations of both $\mathbf{x}(\alpha)$ and $\omega(\alpha)$ about the point on C closest to the target point $\mathbf{x}_0$, obtained by orthogonal projection. The Taylor expansions are used to find a function $\mathcal{H}$ in terms of elementary near-singular basis functions, that approximates the integrand G and can be integrated analytically. The method consists of integrating $\mathcal{H}$ exactly while integrating the remainder $G - \mathcal{H}$ using a basic 4th order trapezoidal rule. In practice, this is equivalent to

adding a correction for each of the basis functions to the 4th order approximation of $\int G$. The order of accuracy depends on the number of terms used to represent $\mathcal{H}$.

Relation to prior work. A number of accurate existing methods use integral values in the domain interior far from the boundary to approximate the near-singular integrals. These include the QBX methods and the integral interpolation methods of [48,37]. The method described here uses function values on the boundary to approximate the integrand. Similarly, the method of [32], concisely described in [33], uses function values on the boundary, within a panel, that are interpolated, resulting in an analytic integral that is evaluated exactly. The present approach, via an application of the geometric series, may be viewed as generalizing the integration of analytic basis functions $1/(z-z_0)^j$, $z = x+iy$, which is a key component in [32] and other works for planar geometries. The present axi-symmetric results, albeit of interest in themselves, may thus also be viewed as a step towards 3D.

Contributions of this work. The method as presented applies to line integrals that appear in planar or axi-symmetric geometries. It requires Taylor expansions of $\mathbf{x}(\alpha)$ and $\omega(\alpha)$, but also expansions of the kernels F. In [28] we considered planar vortex sheet flow, for which these expansions are quite simple. For axi-symmetric Stokes flow, the details are more complex. Thus, the main contributions of this paper are to :

- Present all details necessary in the axi-symmetric Stokes case.
- Evaluate the method on sample axi-symmetric test cases to show that the theoretically predicted convergence rates are achieved.
- Apply the method to a more elaborate example with multiple interfaces that illustrates the importance of accurate near-singular integration in interfacial flow. The example of choice here is the evolution of a double emulsion moving through a constriction.
- The example includes the presence of finite, non-periodic, solid boundaries of the fluid domain. With the exception of [8], most works in the literature focus on periodic smooth interfaces. Here we show the results obtained for nonperiodic boundaries using a representation by a superposition of Stokeslets.

Organization of the paper. The paper is organized as follows. Section 2 presents the boundary integral formulation for axi-symmetric Stokes flow, including all necessary details to find the approximations $\mathcal{H}$. Section 3 presents the key idea of the numerical method, and implementation details. Section 4 presents the numerical results. We first confirm the theoretically predicted convergence rates for test cases, including a spherical test case (§4.1) and the nonperiodic surface representing a nozzle (§4.2). We then present the evolution of the double droplet through the nozzle computed with and without corrections (§4.3). The work is summarized in section 5. All information about the axi-symmetric kernels is given in the appendices.

2 The boundary integrals

This section presents the boundary integrals in axi-symmetric Stokes flow, including all necessary details for the remainder of the paper. For further reference, see [35], [36], [42].

2.1 Boundary integral formulation in axi-symmetric Stokes flow

Stokes equations approximate the incompressible Navier-Stokes equations for a homogeneous fluid with viscosity μ, in the limit of zero Reynolds number. They are given by,

$$\begin{aligned} &0 = -\nabla p + \mu \Delta \mathbf{u} = \nabla \cdot \sigma \ , \quad \nabla \cdot \mathbf{u} = 0 \ , \quad \mathbf{x} \in D \subset \mathbb{R}^3 \\ &\text{with} \quad \sigma_{ik} = -p\delta_{ik} + \mu\Big(\frac{\partial u_i}{\partial x_k} + \frac{\partial u_k}{\partial x_i}\Big) \ , \end{aligned} \tag{2.1}$$

where p is pressure, δ_{ij} is the Kronecker delta function, u_i are the Cartesian coordinates of the velocity $\mathbf{u}$ and σ is the stress tensor.

Here we consider axi-symmetric flow with zero swirl, and represent all variables in axi-symmetric coordinates (z, r). For example, $\mathbf{u} = \langle u_1, u_2 \rangle = \langle u, v \rangle = u\mathbf{e}_z + v\mathbf{e}_r$. The solution to (2.1) in the symmetry plane, $\{(z, r), r \geq 0\}$, can be shown to satisfy the Green's representation formula [22],

$$\frac{1}{\mu}\int_C M(\mathbf{x}, \mathbf{x_o}) \cdot \mathbf{f}(\mathbf{x})\, ds(\mathbf{x}) - \fint_C \mathbf{u}(\mathbf{x}) \cdot Q(\mathbf{x}, \mathbf{x_0}) \cdot \mathbf{n}(\mathbf{x})\, ds(\mathbf{x}) = \begin{cases} \mathbf{u}(\mathbf{x_0}) & \text{if } \mathbf{x_0} \in D \backslash C \\ \frac{1}{2}\mathbf{u}(\mathbf{x_0}) & \text{if } \mathbf{x_0} \in C \\ 0 & \text{if } \mathbf{x_0} \notin D \end{cases} \tag{2.2}$$

given in terms of line integrals over the curve C representing the boundary of the domain D in the z-r plane. The vector $\mathbf{n}$ is the outward normal unit vector, M and Q are the axi-symmetric *Stokeslet* and *Stresslet* tensors, and $\mathbf{f} = \sigma(\mathbf{x}) \cdot \mathbf{n}$, are forces acting on the boundary, obtained from boundary conditions. The first and second integrals on the left hand side of (2.2) are referred to as single- and double-layer potentials and denoted here by $\mathbf{u}^s$ and $\mathbf{u}^d$, respectively. The single layer potential is integrable and continuous across C. The double layer is discontinuous across C and accounts for the jump in (2.2). If $\mathbf{x}_0 \in C$ the double layer is integrable in the principal value sense. The fluid velocity $\mathbf{u}$ given by Eq (2.2) is continuous across C.

Let $\mathbf{x}(\alpha) = \langle z(\alpha), r(\alpha) \rangle$, $\alpha \in [a, b]$ be a parametrization of the curve C. Then,

$$u_i^s(\mathbf{x}_0) = \tfrac{1}{\mu}\textstyle\int_a^b M_{ij}\big(\mathbf{x}(\alpha), \mathbf{x}_0\big)\, f_j(\alpha)\, s_\alpha\, d\alpha \tag{2.3a}$$

$$u_i^d(\mathbf{x}_0) \quad = \textstyle\int_a^b Q_{ijk}[\mathbf{x}(\alpha), \mathbf{x}_0] u_j n_k\, s_\alpha\, d\alpha \tag{2.3b}$$

where $s_\alpha = \sqrt{\dot{z}^2 + \dot{r}^2}$, $\mathbf{n} = (\dot{r}, -\dot{z})/s_\alpha$, and, for each $i = 1, 2$, we use Einstein notation to denote summation over repeated indeces, where $j = 1, 2$, $k = 1, 2$. All components M_{ij}, Q_{ijk} are given in [35,23] in terms of complete elliptic integrals of the first and second kind, and reproduced in Appendix A, for reference. The remainder of this paper focuses on the accurate evaluation of these axi-symmetric single- and double- layer potentials, when $\mathbf{x}_0 \notin C$.

2.2 **The form of the kernels**

The components M_{ij}, Q_{ijk} listed in Appendix A are given in terms of functions I_{jk}. From the expansions of I_{jk} given in (A.3) it follows that,

$$M_{ij}(\mathbf{x},\mathbf{x}_o) = \frac{F_1(\mathbf{x},\mathbf{x}_0)}{|\mathbf{x}-\mathbf{x}_0|^2} + F_0(\mathbf{x},\mathbf{x}_0)\log(|\mathbf{x}-\mathbf{x}_0|) + h.o.t. \quad (2.4a)$$

$$Q_{ijk}(\mathbf{x},\mathbf{x}_o) = \frac{F_2(\mathbf{x},\mathbf{x}_0)}{|\mathbf{x}-\mathbf{x}_0|^4} + \frac{F_1(\mathbf{x},\mathbf{x}_0)}{|\mathbf{x}-\mathbf{x}_0|^2} + F_0(\mathbf{x},\mathbf{x}_0)\log(|\mathbf{x}-\mathbf{x}_0|) + h.o.t. \quad (2.4b)$$

where $h.o.t. = O(|\mathbf{x}-\mathbf{x}_0|)$. That is, the M_{ij}s are less singular than the Q_{ijk}s, and both consist of a sum of near-singular functions of the form (1.1). Due to some symmetry, ($Q_{ijk} = Q_{ikj}$) there are a total of 26 functions F_j describing the near-singular components of the kernels. They are obtained using Mathematica, and listed in Appendix B.

Appendix B also lists the order of the root of each function at $\mathbf{x} = \mathbf{x}_0$. For example, if $\mathbf{x} \approx \mathbf{x}_0$, all functions F_1 and F_2 satisfy,

$$F_1 \sim |\mathbf{x}-\mathbf{x}_0|^2 \ , \quad F_2 \sim |\mathbf{x}-\mathbf{x}_0|^3 \quad (2.5)$$

while F_0 is $O(1)$ in general. That is, F_1 has a double root at $\mathbf{x} = \mathbf{x}_0$, and F_2 has a triple root. This implies that the $p = 2$ integral in both M and Q is integrable if $\mathbf{x}_0 \in C$. Thus the single layer contains only integrable singularities, consistent with the fact that it is continuous across the curve C. Furthermore, the cubic root of F_2 implies that the $p = 4$ integral in Q is integrable in the principal value sense if $\mathbf{x}_0 \in C$, consistent with the fact that the double layer is discontinuous across the surface. In summary, all functions F have a root of sufficiently high order so that the functions are integrable in at least the principal value sense, as expected. The multiplicity of the root will be important below in estimating the size of the integration error of various terms.

The expressions (2.4) for the kernels M and Q are valid for target points $\mathbf{x}_0$ not on the axis, with $r_0 > 0$. For target points $\mathbf{x}_0$ on the axis, with $r_0 = 0$, the radial velocity $v^s = v^d = 0$. An expression for the axial velocity is obtained by taking the limit of (2.3) as $r_0 \to 0$, and given in Appendix C. It follows that,

$$u^s(\mathbf{x}_0) = \frac{1}{\mu}\int_a^b \frac{F_{3/2}(\mathbf{x},\mathbf{x}_0)}{|\mathbf{x}-\mathbf{x}_0|^3}\, s_\alpha\, d\alpha \ , \quad F^{3/2} \sim |\mathbf{x}-\mathbf{x}_0|^3 \ , \quad (2.6a)$$

$$u^d(\mathbf{x}_0) = \int_a^b \frac{F_{5/2}(\mathbf{x},\mathbf{x}_0)}{|\mathbf{x}-\mathbf{x}_0|^5}\, s_\alpha\, d\alpha \ , \quad F^{5/2} \sim |\mathbf{x}-\mathbf{x}_0|^4 \ . \quad (2.6b)$$

In addition, we will use the radial derivatives of the velocities on the axis, also given in appendix C, which have higher order singularities. Thus, for axi-symmetric Stokes flow, we require accurate integration of all cases (1.1) with $p = 2, 3, 4, 5, 7, 9$, as well as the logarithm.

3 Numerical Method

3.1 Key points

We begin with a brief description of the key points of the method introduced in [28]. The generic integrands G of interest are

$$G_{p/2}(\alpha) = \frac{F_{p/2}(\mathbf{x}(\alpha), \mathbf{x}_0)}{|\mathbf{x}(\alpha) - \mathbf{x}_0|^p}\,\omega(\alpha), \tag{3.1a}$$

$$G_0(\alpha) = F_0(\mathbf{x}(\alpha), \mathbf{x}_0)\log|\mathbf{x}(\alpha) - \mathbf{x}_0|\omega(\alpha). \tag{3.1b}$$

The curve $\mathbf{x}(\alpha)$, $\alpha \in [a, b]$ is discretized by a uniform mesh with meshsize $h = (b-a)/n$ and n gridpoints $\alpha_k = a + kh$, $k = 0, \ldots n$. The main idea is to approximate the near-singular functions $G(\alpha)$ to leading order for $d \ll 1$ by a function $\mathcal{H}(\alpha)$ that captures the near-singularity and can be integrated exactly. We then approximate the integral of interest by,

$$\int G = \int (G - \mathcal{H} + \mathcal{H}) \tag{3.2a}$$

$$\approx T_4[G - \mathcal{H}] + \int \mathcal{H} \tag{3.2b}$$

$$= T_4[G] + \Big(\int \mathcal{H} - T_4[\mathcal{H}] \Big) \tag{3.2c}$$

$$= T_4[G] + E_4[\mathcal{H}] := T^*[G]\ . \tag{3.2d}$$

In (3.2a), we add and subtract the approximation from G. In (3.2b), we approximate the smoother difference $G - \mathcal{H}$ by a fourth order generalized trapezoid rule T_4, while integrating $\mathcal{H}$ exactly. In (3.2c), we rearrange terms using the linearity of T_4. The last equality (3.2d) summarizes the method as implemented: it consists of adding the correction $E_4[\mathcal{H}] := \int \mathcal{H} - T_4[\mathcal{H}]$ to the trapezoid approximation of the uncorrected integral. The corrected quadrature is denoted by $T^*[G]$ in §3.4 below. In some cases below we replace T_4 by the sixth order rule T_6, in order to reduce the background errors, where,

$$T_4[f] := h{\sum_{k=0}^{n}}' f(\alpha_k) - \frac{h^2}{12}[f'(b) - f'(a)]\ , \tag{3.3a}$$

$$T_6[f] := h{\sum_{k=0}^{n}}' f(\alpha_k) - \frac{h^2}{12}[f'(b) - f'(a)] + \frac{h^4}{720}[f'''(b) - f'''(a)]\ . \tag{3.3b}$$

The prime on the summation denotes that the first and last term in the sum are weighted by 1/2. This basic approach follows that of earlier work by the author and coworkers to approximate singular integrals in [26,27,30].

The approximation $\mathcal{H}$ is obtained by first approximating both the numerator and the denominator in G using Taylor series of $\mathbf{x}(\alpha)$ and $\omega(\alpha)$ about a basepoint α_b. The basepoint is chosen so that $\mathbf{x}(\alpha_b)$ is the orthogonal projection of $\mathbf{x}_0$ onto C, as illustrated in figure 3. An application of the geometric series then yields a

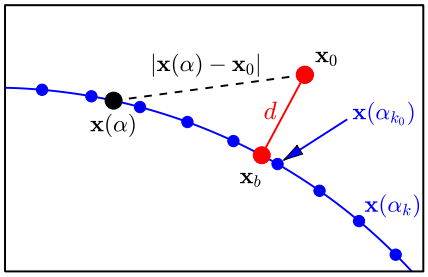

Fig. 3 Projection to basepoint $\mathbf{x}_b = \mathbf{x}(\alpha_b)$ of $\mathbf{x}_0$ onto curve $\mathbf{x}(\alpha)$, which is discretized by points $\mathbf{x}(\alpha_k)$. The point $\mathbf{x}(\alpha_{k_0})$ is the gridpoint closest to $\mathbf{x}_b$.

converging series expansion of G in terms of basis functions H_{jk} which capture the near-singular behaviour of G and can be integrated exactly,

$$G = \sum_{j=0}^{\infty}\sum_{k=0}^{\infty} c'_{jk} H_{jk} \ , \qquad H_{jk} = \begin{cases} \dfrac{\hat{\alpha}^k}{(d^2+c^2\hat{\alpha}^2)^j} \ , & j \geq 1 \\ \hat{\alpha}^k \log(d^2+c^2\hat{\alpha}^2) \ , & j = 0 \end{cases} , \tag{3.4}$$

where $\hat{\alpha} = \alpha - \alpha_b$. The coefficients c'_{jk} depend on α_b and on the function G, given in turn by the functions $F_{p/2}, \mathbf{x}(\alpha), \omega(\alpha)$. The next section explains in more detail how to obtain the c'_{jk}s.

The approximation $\mathcal{H}$ is then obtained by truncating the series expansion (3.4) of G. To determine where to truncate the series for a desired order of accuracy in $\int G$, we use the upper bounds for the error $E[H_{jk}] = \int H_{jk} - T_4[H_{jk}]$ made in integrating H_{jk} by the trapezoid rule, derived in [28]. They are given by,

$$E_4[H_{jk}] = \begin{cases} O(hd^{k-2j}) \ , & j \geq 1 \\ O(h\log d) \ , & j = 0, k = 0 \\ O(h^{k+1}) \ , & j = 0, k > 0 \end{cases} , \tag{3.5}$$

in addition to an $O(h^4)$ term (or $O(h^4 \log h)$ if $j = 0$) for $k \geq 2j+4$. To illustrate, the details on how to obtain $\mathcal{H}$ are presented next for an example.

3.2 **The approximation $\mathcal{H}$**

Suppose we wish to approximate $\int G_2$ to $O(h^3)$. We need to find $\mathcal{H} \approx G$, where $G = G_2$. We begin by finding the orthogonal projection $\mathbf{x}_b = \mathbf{x}(\alpha_b)$ of $\mathbf{x}_0$ onto the curve C (see figure 3). This step determines $d = |\mathbf{x}_0 - \mathbf{x}_b|$ and the basepoint α_b. We then approximate

$$\mathbf{x}(\alpha) = \mathbf{x}_b + \dot{\mathbf{x}}_b\hat{\alpha} + \ddot{\mathbf{x}}_b\frac{\hat{\alpha}^2}{2} + \dddot{\mathbf{x}}_b\frac{\hat{\alpha}^3}{6} + O(\hat{\alpha}^4) \tag{3.6a}$$

$$\omega(\alpha) = \omega_b + \dot{\omega}_b\hat{\alpha} + \ddot{\omega}_b\frac{\hat{\alpha}^2}{2} + O(\hat{\alpha}^3) \tag{3.6b}$$

where the subscript b denotes evaluation at α_b, and $\hat{\alpha} = \alpha - \alpha_b$. Note that ω is approximated to a lower order than $\mathbf{x}$. These expressions are substituted into the

expression for the numerator F_2. Since F_2, given in Appendix B, is in all cases a polynomial, we multiply all terms to obtain

$$F_2(\mathbf{x},\mathbf{x}_0)\,\omega(\alpha) = c_0 + c_1\hat{\alpha} + c_2\hat{\alpha}^2 + c_3\hat{\alpha}^3 + c_4\hat{\alpha}^4 + c_5\hat{\alpha}^5 + O(\hat{\alpha}^6 + d\hat{\alpha}^5 + d^2\hat{\alpha}^4 + d^3\hat{\alpha}^3) \tag{3.7}$$

Here, we used the fact that F_2 has a triple root at $\mathbf{x} = \mathbf{x}_0$ and thus $c_0 = O(d^3)$, $c_1 = O(d^2)$, and $c_2 = O(d)$. The last term denotes that the error in the series approximation of F_2 is a sum of terms of the given order.

The denominator of G is expanded as

$$|\mathbf{x}(\alpha) - \mathbf{x}_0|^2 = d^2 + c^2\hat{\alpha}^2 + e_3\hat{\alpha}^3 + e_4\hat{\alpha}^4 + O(\hat{\alpha}^5) \tag{3.8}$$

where

$$c^2 = |\dot{\mathbf{x}}_b|^2 + \ddot{\mathbf{x}}_b \cdot (\mathbf{x}_b - \mathbf{x}_0)\ , \tag{3.9a}$$

$$e_3 = \dot{\mathbf{x}}_b \cdot \ddot{\mathbf{x}}_b + \frac{1}{3}(\mathbf{x}_b - \mathbf{x}_0) \cdot \dddot{\mathbf{x}}_b = \tilde{e}_3 + O(d)\ , \tag{3.9b}$$

$$\tilde{e}_3 = \dot{\mathbf{x}}_b \cdot \ddot{\mathbf{x}}_b\ , \tag{3.9c}$$

$$e_4 = \dot{\mathbf{x}}_b \cdot \dddot{\mathbf{x}}_b/3 + \ddot{\mathbf{x}}_b \cdot \ddot{\mathbf{x}}_b/4 + (\mathbf{x}_b - \mathbf{x}_0) \cdot \ddddot{\mathbf{x}}_b/12 = \tilde{e_4} + O(d)\ , \tag{3.9d}$$

$$\tilde{e}_4 = \dot{\mathbf{x}}_b \cdot \dddot{\mathbf{x}}_b/3 + \ddot{\mathbf{x}}_b \cdot \ddot{\mathbf{x}}_b/4. \tag{3.9e}$$

Here, the low order approximations $\tilde{e}_3$ and $\tilde{e}_4$ of e_3 and e_4 are included for later reference. A linear term $\alpha - \alpha_b$ does not appear in (3.8) since $\mathbf{x}_b$ is defined to be the orthogonal projection of $\mathbf{x}_0$ onto the sheet, and $\dot{\mathbf{x}}_b$ is tangent to the sheet, so that $\dot{\mathbf{x}}_b \cdot (\mathbf{x}_b - \mathbf{x}_0) = 0$. It is not necessary to ensure that the linear term vanishes, but it simplifies the resulting expressions for H_{jk} and thereby simplifies the corresponding integrals. In addition, in the presence of a linear term one must be careful to avoid division by zero that can occur after truncation. In general, finding the orthogonal projection accurately is easy, as described in §3.3, and no advantage has been found to considering the more general inclusion of a linear term. We do require that $c^2 > 0$. In [28] we show that this is always the case if C is piecewise linear (such as the nozzle considered below). If C is curved but uniformly discretized in arclength (such as the evolving drops below), we show that $c^2 > 0$ whenever $\mathbf{x}_0$ is "outside" of the curve, or, if it is "inside", when d is less than the radius R_{osc} of the osculating circle, where the inside is defined to be the side of the osculating circle.

Next, we apply the geometric series to obtain an expansion of G in terms of H_{jk} and order the terms with respect to the corresponding bounds for $E[H_{jk}]$ given in (3.5):

$$\begin{aligned}
G_2(\alpha) =& \frac{F_2(\mathbf{x}(\alpha),\mathbf{x}_0)}{|\mathbf{x}(\alpha) - \mathbf{x}_0|^4}\,\omega(\alpha) \\
=& \frac{c_0 + c_1\hat{\alpha} + c_2\hat{\alpha}^2 + c_3\hat{\alpha}^3 + c_4\hat{\alpha}^4 + c_5\hat{\alpha}^5 + O(\hat{\alpha}^6 + d\hat{\alpha}^5 + d^2\hat{\alpha}^4 + d^3\hat{\alpha}^3)}{(d^2 + c^2\hat{\alpha}^2 + e_3\hat{\alpha}^3 + e_4\alpha^4 + O(\hat{\alpha}^5))^2} \\
=& \frac{c_0 + c_1\hat{\alpha} + c_2\hat{\alpha}^2 + c_3\hat{\alpha}^3 + c_4\hat{\alpha}^4 + c_5\hat{\alpha}^5 + O(\hat{\alpha}^6 + d\hat{\alpha}^5 + d^2\hat{\alpha}^4)}{(d^2 + c^2\hat{\alpha}^2)^2} \times \\
& \left[1 - 2\frac{e_3\hat{\alpha}^3 + e_4\hat{\alpha}^4 + O(\hat{\alpha}^5)}{d^2 + c^2\hat{\alpha}^2} + 3\frac{e_3^2\hat{\alpha}^6 + O(\hat{\alpha}^7)}{(d^2 + c^2\hat{\alpha}^2)^2} + \frac{O(\hat{\alpha}^9)}{(d^2 + c^2\hat{\alpha}^2)^3}\right]
\end{aligned}$$

$$
\left.
\begin{aligned}
&= \underbrace{\frac{c_0 + c_1\hat{\alpha} + c_2\hat{\alpha}^2 + c_3\hat{\alpha}^3}{(d^2 + c^2\hat{\alpha}^2)^2}}_{E[\cdot]=O(h/d)} + \underbrace{\frac{c_4\hat{\alpha}^4}{(d^2 + c^2\hat{\alpha}^2)^2} - 2e_3\frac{(c_0 + c_1\hat{\alpha} + c_2\hat{\alpha}^2 + c_3\hat{\alpha}^3)\hat{\alpha}^3}{(d^2 + c^2\hat{\alpha}^2)^3}}_{E[\cdot]=O(h)} \\
&- \underbrace{2\tilde{e}_3\frac{c_4\hat{\alpha}^7}{(d^2 + c^2\hat{\alpha}^2)^3} - 2\tilde{e}_4\frac{(c_0 + c_1\hat{\alpha} + c_2\hat{\alpha}^2 + c_3\hat{\alpha}^3)\hat{\alpha}^4}{(d^2 + c^2\hat{\alpha}^2)^3}}_{E[\cdot]=O(hd)} \\
&+ \underbrace{\frac{c_5\hat{\alpha}^5}{(d^2 + c^2\hat{\alpha}^2)^2} + 3\tilde{e}_3^2\frac{(c_0 + c_1\hat{\alpha} + c_2\hat{\alpha}^2 + c_3\hat{\alpha}^3)\hat{\alpha}^6}{(d^2 + c^2\hat{\alpha}^2)^4}}_{E[\cdot]=O(hd)} \\
&+ \underbrace{\frac{O(d^2\hat{\alpha}^4 + d\hat{\alpha}^5 + \hat{\alpha}^6)}{(d^2 + c^2\hat{\alpha}^2)^2} + \frac{O(d^3\hat{\alpha}^5 + d^2\hat{\alpha}^6 + d\hat{\alpha}^7 + \hat{\alpha}^8)}{(d^2 + c^2\hat{\alpha}^2)^3} + \frac{O(d^3\hat{\alpha}^7 + \cdots + \hat{\alpha}^{10})}{(d^2 + c^2\hat{\alpha}^2)^4}}_{E[\cdot]=O(hd^2+h^4)}
\end{aligned}
\right\} \begin{array}{l} \mathcal{H}_1 \\ \\ \\ \mathcal{H}_2 \\ \\ \\ \\ \\ \end{array}
\tag{3.10}
$$

Thus it becomes clear how to approximate G to obtain a desired order of accuracy: If $G \approx \mathcal{H}_1$ where $\mathcal{H}_1$ consists of all terms with error bigger than $O(hd)$, as indicated in (3.10), then the resulting integral is approximated to within $O(hd + h^4)$. Since the approximation is applied if $d = O(h)$, this yields an overall $O(h^2)$ method. If $G \approx \mathcal{H}_1 + \mathcal{H}_2$, where $\mathcal{H}_2$ consists of all remaining terms with error bigger than $O(hd^2)$, then the resulting integral is approximated to within $O(hd^2 + h^4)$, or $O(h^3)$. Moreover, if all derivatives at $\mathbf{x}_b$ are computed with sufficient accuracy, the approximation errors vanish as $d \to 0$, up to the background pointwise error of $O(h^4)$.

If higher order approximations are desired, they can be obtained using more terms in the expansions of G and a higher order background Trapezoid approximation, if necessary.

Table 1 summarizes the result for all near-singular integrals present in axisymmetric Stokes flow: the functions $G_{p/2}$ with $p = 0, 1, 2, 3, 4, 5$. For each G, $\mathcal{H}_1$ and $\mathcal{H}_2$ are indicated where $G \approx \mathcal{H}_1$ yields an $O(h^2)$ method, and $G \approx \mathcal{H}_1 + \mathcal{H}_2$ yields an $O(h^3)$ method. Here, we used the fact that in Stokes flow all G_1 have a second order root at $\mathbf{x} = \mathbf{x}_0$. Furthermore, for the functions $G_{3/2}$ and $G_{5/2}$ that appear when the target point lies on the axis, the numerator is odd and the denominator even, thereby greatly simplifying the resulting approximation. The functions $G_{7/2}$ and $G_{9/2}$ given in Appendix C are handled similarly.

Finally, note that the $O(h^3)$ order approximation requires

- for G_2: 3 derivatives in $\mathbf{x}$, 2 in ω,
- for G_1: 2 derivatives in $\mathbf{x}$, 1 in ω, (in view of the double root of F_1)
- for G_0: 1 derivatives in $\mathbf{x}$, 1 in ω.

Similarly, one can extend these expansions to obtain an approximation of order $O(h^m)$ that requires

- for G_2: m derivatives in $\mathbf{x}$, $m-1$ in ω,

G_1	$\dfrac{F_1(\mathbf{x}(\alpha),\mathbf{x}_0)}{\lvert\mathbf{x}(\alpha)-\mathbf{x}_0\rvert^2}\,\omega(\alpha) = \dfrac{c_0+c_1\hat\alpha+c_2\hat\alpha^2+c_3\hat\alpha^3+O(\hat\alpha^4+d\hat\alpha^3+d^2\hat\alpha^2)}{d^2+c^2\hat\alpha^2+e_3\hat\alpha^3+O(\hat\alpha^4)}$
	$\approx \dfrac{c_0+c_1\hat\alpha+c_2\hat\alpha^2+c_3\hat\alpha^3}{d^2+c^2\hat\alpha^2}\Big[1-\dfrac{\tilde e_3\hat\alpha^3}{d^2+c^2\hat\alpha^2}\Big]$
$\mathcal{H}_1$	$\approx \dfrac{c_0+c_1\hat\alpha+c_2\hat\alpha^2}{d^2+c^2\hat\alpha^2}$
$\mathcal{H}_2$	$-\tilde e_3\dfrac{c_0\hat\alpha^3+c_1\hat\alpha^4+c_2\hat\alpha^5}{(d^2+c^2\hat\alpha^2)^2} + \dfrac{c_3\hat\alpha^3}{d^2+c^2\hat\alpha^2}$
G_2	$\dfrac{F_2(\mathbf{x}(\alpha),\mathbf{x}_0)}{\lvert\mathbf{x}(\alpha)-\mathbf{x}_0\rvert^4}\,\omega(\alpha) = \dfrac{c_0+c_1\hat\alpha+c_2\hat\alpha^2+c_3\hat\alpha^3+c_4\hat\alpha^4+c_5\hat\alpha^5+O(\hat\alpha^6+d\hat\alpha^5+d^2\hat\alpha^4+d^3\hat\alpha^3)}{(d^2+c^2\hat\alpha^2+e_3\hat\alpha^3+e_4\hat\alpha^4+O(\hat\alpha^5))^2}$
	$\approx \dfrac{c_0+c_1\hat\alpha+c_2\hat\alpha^2+c_3\hat\alpha^3+c_4\hat\alpha^4+c_5\hat\alpha^5}{(d^2+c^2\hat\alpha^2)^2}\Big[1-2\dfrac{e_3\hat\alpha^3+\tilde e_4\hat\alpha^4}{d^2+c^2\hat\alpha^2}+3\dfrac{e_3^2\hat\alpha^6}{(d^2+c^2\hat\alpha^2)^2}\Big]$
$\mathcal{H}_1$	$\approx \dfrac{c_0+c_1\hat\alpha+c_2\hat\alpha^2+c_3\hat\alpha^3+c_4\hat\alpha^4}{(d^2+c^2\hat\alpha^2)^2} - 2e_3\dfrac{c_0\alpha^3+c_1\hat\alpha^4+c_2\hat\alpha^5+c_3\hat\alpha^6}{(d^2+c^2\hat\alpha^2)^3}$
$\mathcal{H}_2$	$-2\tilde e_3\dfrac{c_4\hat\alpha^7}{(d^2+c^2\hat\alpha^2)^3} - 2\tilde e_4\dfrac{(c_0+c_1\hat\alpha+c_2\hat\alpha^2+c_3\hat\alpha^3)\hat\alpha^4}{(d^2+c^2\hat\alpha^2)^3}$
	$+\dfrac{c_5\hat\alpha^5}{(d^2+c^2\hat\alpha^2)^2} + 3\tilde e_3^2\dfrac{(c_0+c_1\hat\alpha+c_2\hat\alpha^2+c_3\hat\alpha^3)\hat\alpha^6}{(d^2+c^2\hat\alpha^2)^4}$
G_0	$F(\mathbf{x}(\alpha),\mathbf{x}_0)\omega(\alpha)\log\lvert\mathbf{x}(\alpha)-\mathbf{x}_0\rvert^2 = \big[c_0+c_1\hat\alpha+O(\hat\alpha^2)\big]\,\log\big(d^2+c^2\hat\alpha^2+e_3\hat\alpha^3+O(\hat\alpha^4)\big)$
	$\approx \big[c_0+c_1\hat\alpha\big]\big[\log(d^2+c^2\hat\alpha^2)+\dfrac{e_3\hat\alpha^3}{d^2+c^2\hat\alpha^2}\big]$
$\mathcal{H}_1$	$\approx c_0\log(d^2+c^2\hat\alpha^2)$
$\mathcal{H}_2$	$+c_1\hat\alpha\log(d^2+c^2\hat\alpha^2)+\tilde e_3\dfrac{c_0\hat\alpha^3}{d^2+c^2\hat\alpha^2}$
$G_{\frac32}$	$\dfrac{F_{\frac32}(\mathbf{x}(\alpha),\mathbf{x}_0)}{\lvert\mathbf{x}(\alpha)-\mathbf{x}_0\rvert^3}\,\omega(\alpha) = \dfrac{c_1\hat\alpha+c_3\hat\alpha^3+O(\hat\alpha^5+d\hat\alpha^4+d^2\hat\alpha^3+d^3\hat\alpha^2)}{(d^2+c^2\hat\alpha^2+O(\hat\alpha^4))^{3/2}}$
$\mathcal{H}_1$	$\approx \dfrac{c_1\hat\alpha+c_3\hat\alpha^3}{(d^2+c^2\hat\alpha^2)^{3/2}}$
$\mathcal{H}_2$	$+0$
$G_{\frac52}$	$\dfrac{F_{\frac52}(\mathbf{x}(\alpha),\mathbf{x}_0)}{\lvert\mathbf{x}(\alpha)-\mathbf{x}_0\rvert^5}\,\omega(\alpha) = \dfrac{c_1\hat\alpha+c_3\hat\alpha^3+c_5\hat\alpha^5+O(\hat\alpha^7+..+d^4\hat\alpha^3)}{(d^2+c^2\hat\alpha^2+e_4\hat\alpha^4+O(\hat\alpha^5))^{5/2}}$
	$\approx \dfrac{c_1\hat\alpha+c_3\hat\alpha^3+c_5\hat\alpha^5}{(d^2+c^2\hat\alpha^2)^{5/2}}\Big[1-\dfrac52\dfrac{\tilde e_4\hat\alpha^4}{d^2+c^2\hat\alpha^2}\Big]$
$\mathcal{H}_1$	$\approx \dfrac{c_1\hat\alpha+c_3\hat\alpha^3+c_5\hat\alpha^5}{(d^2+c^2\hat\alpha^2)^{5/2}}$
$\mathcal{H}_2$	$-\dfrac52\tilde e_4\dfrac{(c_1\hat\alpha+c_3\hat\alpha^3)\hat\alpha^4}{(d^2+c^2\hat\alpha^2)^{7/2}}$

Table 1 Summary of the approximations $G \approx \mathcal{H}_1 + \mathcal{H}_2$. In each case, the approximations $G \approx \mathcal{H}_1$ and $G \approx \mathcal{H}_1 + \mathcal{H}_2$ yield an $O(h^2)$ and $O(h^3)$ approximations of $\int G$, respectively. For the $O(h^2)$ method, it is sufficient to replace e_3 by its dominant term $\tilde e_3$ in $\mathcal{H}_1$. Throughout, $\hat\alpha = \alpha - \alpha_p$.

– for G_1: $m-1$ derivatives in $\mathbf{x}$, $m-2$ in ω, (in view of the double root of F_1)
– for G_0: $m-2$ derivatives in $\mathbf{x}$, $m-2$ in ω.

Note that Table 1 lists the coefficients c'_{jk} in terms of the coefficients c_j, e_3 and e_4.

In section 4 we show results using the $O(h^2)$ and the $O(h^3)$ versions described by Table 1, as well as an $O(h^4)$ version obtained by keeping more terms in the expansion of G. For the necessary details in this latter case we refer the reader to the code posted publicly on the github repository [29].

3.3 **Implementation**

The method is implemented as follows, where, for illustration, we describe the $O(h^3)$ method, although the steps easily generalize to the $O(h^4)$ version used below. Steps:
Step 1: Compute $T_4[G]$.
Step 2: If $\mathbf{x}_0$ is too close to C then
a) find α_b, d, and the closest gridpoint α_{k_0} to α_b
b) find all necessary values at α_b: $\mathbf{x}_b, \dot{\mathbf{x}}_b, \ddot{\mathbf{x}}_b, \dddot{\mathbf{x}}_b$, $\omega_b, \dot{\omega}_b, \ddot{\omega}_b$
c) find all necessary coefficients c^2, e_k, c_k, as described in §3.2
d) compute all necessary $E_4[H_{jk}]$
e) correct $\int G \approx T_4[G] + \sum c'_{jk} E_4[H_{jk}]$ where c'_{jk} are given in Table 1.

Several notes are in order:

(i) Definition of "too close": In the calculations in section 3 below, the correction is applied when $d < \min(5\Delta s, R_{osc}/2)$, where Δs is the spacing between the two gridpoints closest to $\mathbf{x}_0$. This criterion is consistent with the criterion used by Klöckner et al [21], who considered the "high-accuracy region" in which standard quadratures give good results and no correction is necessary to be at a distance of $5h \sim 5\Delta s$.

(ii) In step 2a: In general, such as for moving surfaces, α_b is found by first fitting a cubic polynomial to the data at the gridpoints in $[\alpha_{k_0-1}, \alpha_{k_0+2}]$, and then applying a few Newton iterations to find the point at which $(\mathbf{x}_0 - \mathbf{x}(\alpha_b)) \cdot \dot{\mathbf{x}}(\alpha_b) = 0$.
For prescribed boundaries, for which an expression for $\mathbf{x}(\alpha)$ is known, α_b can often be found exactly in one step.
If $\mathbf{x}_0$ does not have an orthogonal projection onto C, for example, if it lies to the right of the tip of the nozzle, yet is close enough to require correction, we use the closest point on C as $\mathbf{x}_b$. This does not introduce a linear term into (3.8) since we impose $\dot{\mathbf{x}}_b = 0$ at tips by sufficiently bunching the discretization points.

(iii) In step 2b: the highest derivatives $\dddot{\mathbf{x}}_b$, $\ddot{\omega}_b$, need to be evaluated to $O(h)$ only. The next highest to $O(h^2)$, etc. They are obtained by differentiating a sufficiently high order interpolant of the nearest points.

(iv) In step 2d: It is only necessary to evaluate $E[H_{jk}]$ over an interval centered at α_{k_0},

$$I = [\alpha_{k_0 - n_{win}}, \alpha_{k_0 + n_{win}}] \ , \tag{3.11}$$

where typically $n_{win} = 10 - 40$, depending on the desired accuracy [28], at a cost of $O(n_{win})$ per basis function. Here, as before, α_k is the kth gridpoint.

However, for simplicity and since the cost is minimal, the results in §4 are computed using $I = [a, b]$.
All $E[H_{jk}] = \int H_{jk} - T[H_{jk}]$ are evaluated by computing $\int H_{jk}$ and $T[H_{jk}]$ and then subtracting them. This method works well as long as each term is not large, as discussed below in §3.5. The antiderivatives of all basis functions H_{jk} are obtained in Mathematica. Results of a sample Mathematica notebook is included in the supplementary materials to this paper.

(v) In step 2e: For the $O(h^3)$ method, the sum consists of 3, 7 and 15 terms for G_0, G_1 and G_2 respectively.

3.4 **Correction near Axis**

If the interface meets the symmetry axis at a point $\mathbf{x}_{ax}$, such as in the case of drops, the approximation above loses accuracy for target points near $\mathbf{x}_{ax}$, and an additional correction is necessary. This difficulty is a well-known problem in axi-symmetric geometry [7,25–27,30], caused by unbounded derivatives of the integrands at the endpoints of integration, in the limit as $\mathbf{x}_0 \to \mathbf{x}_{ax}$. Here we follow the approach in [30] for singular integrals, and approximate the integrand G by a simpler function B that is integrated over a short interval near $\mathbf{x}_{ax}$ with high accuracy using Tschebichev points. We then add the following correction

$$\int G = \int (G - B + B) \approx T^*[G - B] + \int B = T^*[G] + E^*[B] \ , \tag{3.12}$$

where

$$E^*[f] = \int f - T^*[f] \ , \quad T^*[f] = T_4[f] + E_4[\mathcal{H}_f] \ . \tag{3.13}$$

This approach works well, giving uniform convergence outside a small remaining neighbourhood of $\mathbf{x}_{ax}$, as will be seen below. The function B is obtained by approximating $\mathbf{x}(\alpha)$ by a quintic polynomial with appropriate symmetry about $\mathbf{x}_{ax}$, and approximating the forces f_1, f_2 or u, v by quadratic functions. In [30], the integral of the corresponding approximation could be precomputed due to scaling of the singular integrals, at a cost of $O(1)$ per timestep. For the near-singular integrals considered here that scaling is absent, which is why the integral has to be computed accurately using Tchebishev points at a cost of $O(n)$ per timestep. In practice, this correction is rarely needed since the near-interface situation generally occurs away from the axis.

3.5 **Avoiding accumulation of roundoff error**

There are many sources of large roundoff error in these axisymmetric calculations. Foremost is the fact that the near-singular axisymmetric integrands consist of sums of large components that almost cancel each other. The leading order non-integrable singularity must cancel as $\mathbf{x}_0$ approaches the interface C, since the expressions are integrable in at least the principal value sense when $\mathbf{x}_0 \in C$. This problem is remedied by, in essence, replacing terms such as the left-hand side of the following equation by the right-hand side,

$$x^3 - 3x^2 x_0 + 3x x_0^2 - x_0^3 = (x - x_0)^3 \ , \tag{3.14}$$

as in [30]. In addition, we replace the difference $\big(E(k)-1\big)$ by well-known asymptotic approximations if $k \approx 1$. Note that in planar or fully 3D geometries this issue does not occur since the numerators of all near-singular terms are already in factored form, as in the right hand side of equation (3.14).

Secondly, standard functions to evaluate elliptic integrals lose accuracy if the argument is close to one. For example, MATLABs function `ellipke` with argument $k^2 = 1 - 10^{-7}$ returns only 10 correct significant digits. For $k^2 = 1 - 10^{-13}$, it returns only 4 correct digits, and the problem worsens as $1-k^2$ decreases. We use a routine based on consecutive arithmetic-geometric means, that returns 15 or more correct digits for arbitrarily small values of $1 - k^2$. The improvement is obtained by replacing the left-hand side of the following equation by the right-hand side,

$$(x - x_0)^2 - (x + x_0)^2 = 4xx_0 \ . \tag{3.15}$$

Finally, the present method consists of obtaining accurate results by adding a correction to a bad result. If the bad error is large, the correction is large, leading to subtraction of two large numbers to yield a more accurate much smaller number, which leads to loss of significant digits. This issue is resolved by noting that the error in the bad result

$$T[G] \approx h \sum G_k \tag{3.16}$$

is large when the distance $|\mathbf{x}_0 - \mathbf{x}(\alpha_{k_0})| \ll 1$ for some index k_0. In that case

$$|G_{k_0}| \gg \max_{k \neq k_0} |G_k| \ . \tag{3.17}$$

That is, one term in the sum accounts for the large value of the error in the bad result. Similarly, the correction is large due to the contribution of one term in the sum $h \sum H_k$, namely, hH_{k_0}. The problem is resolved by noting that if $|\mathbf{x}_0 - \mathbf{x}(\alpha_{k_0})| \ll 1$, the approximation of $G_{k_0} - H_{k_0}$ given by Table 1 is small, and highly accurate. We thus replace the difference of the two large numbers by the small asymptotic approximation,

$$G_{k_0} - H_{k_0} \approx rest(\alpha_{k_0}) \tag{3.18}$$

and eliminate the loss of precision due to roundoff. Here the remainder *rest* is obtained in Mathematica, as shown in the sample file given in the supplementary materials. This method was implemented and tested, although not needed for the present results since the closest distance of a target point to a gridpoint, approximately 10^{-4}, did not yield sufficiently large corrections to contaminate the results.

4 Numerical Results

4.1 Spherical drop

The corrected trapezoidal quadrature described above is applied to a simple test case of a spherical drop, given by $\mathbf{x}(\alpha) = \langle -\cos\alpha, \sin\alpha \rangle$, $\alpha \in [0, \pi]$, and discretized uniformly by n points with meshsize $h = \pi/n$. The single and double layer velocity components are computed for sample prescribed functions, $f_1(\alpha) = \cos\alpha$, $f_2(\alpha) =$

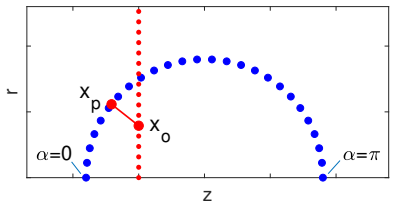

Fig. 4 Discretization of spherical drop by $n = 25$ points (blue). The red dotted line represents a set of target points $\mathbf{x}_0$. The projection $\mathbf{x}_b$ for a sample target point is indicated.

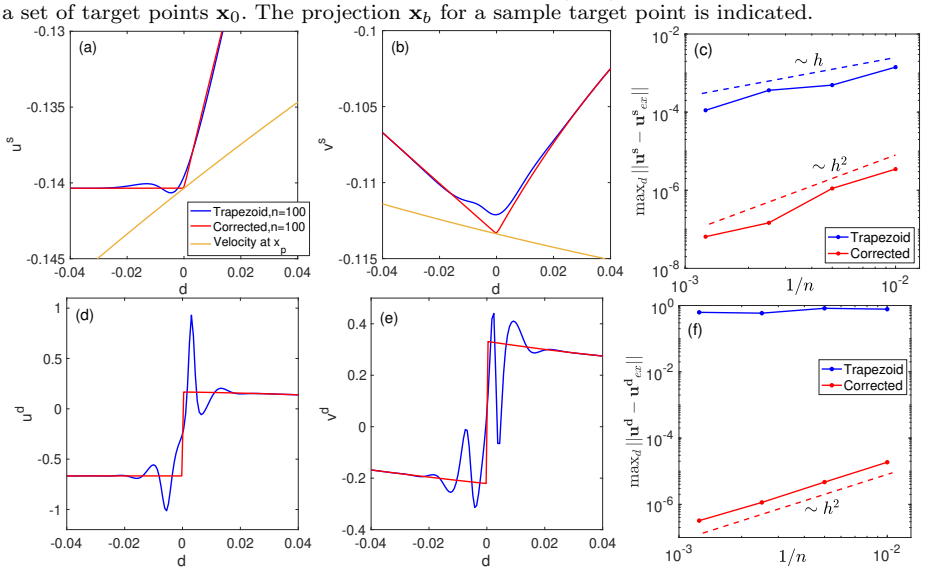

Fig. 5 (a,b,d,e) Computed single and double layer components (u^s, v^s) and (u^d, v^d) along red line in Figure 4, vs the signed distance d from the projection. The trapezoid T_4 results (blue) and the corrected $O(h^2)$ results (red) are shown. For reference, the yellow curve in (a,b) shows the velocity at $\mathbf{x}_b$ on the surface. (c,f) Maximum error along fine grid on red line, with trapezoidal (blue) and corrected values (red), vs. $1/n = h/\pi$. The dashed lines have the indicated slopes.

$\sin\alpha, u(\alpha) = \cos\alpha, v(\alpha) = \sin\alpha$, using the $O(h^2)$, $O(h^3)$, and $O(h^4)$ versions of the method.

Figure 4 shows the discretization by $n = 50$ points (blue) and a dotted line (red), representing a set of target points $\mathbf{x}_0$. Figures 5(a,b,d,e) plot the components of $\mathbf{u}^s = \langle u^s, v^s \rangle$ and $\mathbf{u}^d = \langle u^d, v^d \rangle$ along this red line, as a function of the distance d from $\mathbf{x}_0$ to the projection, computed without corrections (blue) and with the $O(h^2)$ correction (red), using $n = 100$. The yellow curve in (a,b) shows the values of $\mathbf{u}^s$ at the projection $\mathbf{x}_b$ on the interface. These values are given by a singular integral that is evaluated using the methods of [40,30]. The corrected single layer components in figures (a,b) are seen to be continuous across the interface, and agree with the singular integral values on the interface. The corrected double layer components in figures (d,e) recover the discontinuity across the surface.

Figures (c,f) plot the maximum errors $|\mathbf{u}^s - \mathbf{u}^s_{ex}|$ and $|\mathbf{u}^d - \mathbf{u}^d_{ex}|$ over a fine mesh along the red line, using $n = 100, 200, 400, 800$, where the reference values $\mathbf{u}_{ex}$ are computed using $n = 1600$. The corrected values (red) are observed to converge

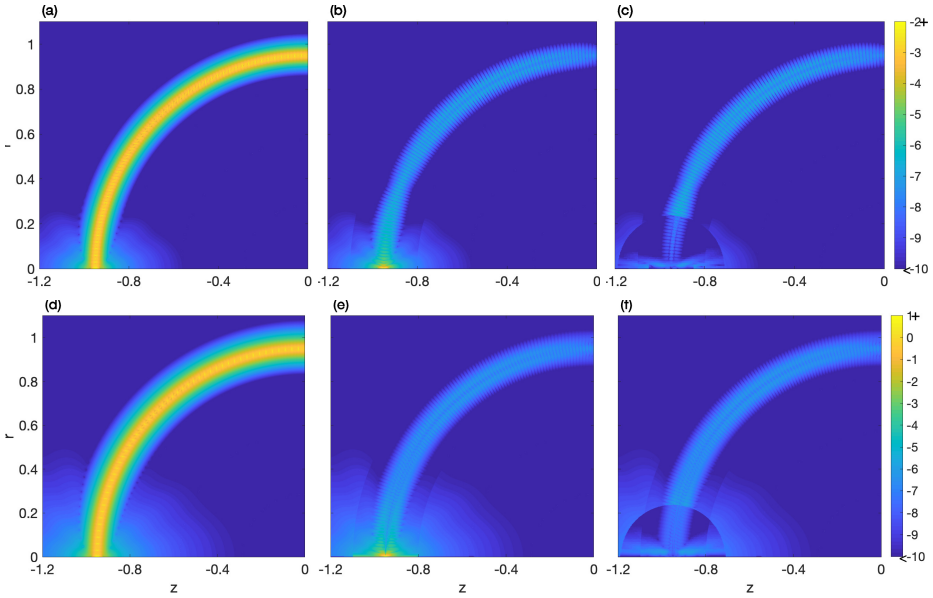

Fig. 6 Pointwise errors on a fine grid in the region shown, computed with the $O(h^3)$ method and $n = 100$. The reference values $\mathbf{u}_{ex}$ are computed with $n = 1600$. (a,b,c) Single layer component $|\mathbf{u}^s - \mathbf{u}^s_{ex}|$. (d,e,f) Double layer component $|\mathbf{u}^d - \mathbf{u}^d_{ex}|$. Left column (a,d): uncorrected trapezoid results $T_6[G]$. Middle column (b,e): corrected $O(h^3)$ results $T_6[G] + E_6[\mathcal{H}] = T^*[G]$. Right column (c,f): additional correction near axis, $T^*[G] + E^*[B]$.

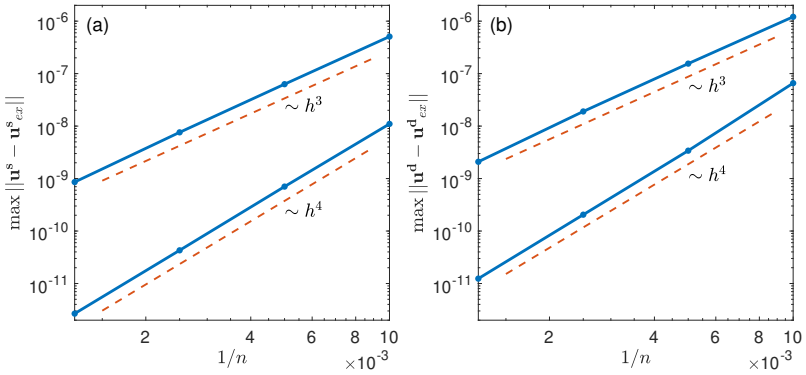

Fig. 7 Maximum errors in the corrected velocities computed with the $O(h^3)$ and the $O(h^4)$ method, vs $1/n = h/\pi$. The maximum is taken over all grid points for the $O(h^3)$ method, and over $r > 0.05$ for the $O(h^4)$ method. (a) Single layer component $\max|\mathbf{u}^s - \mathbf{u}^s_{ex}|$. (b) Double layer component $\max|\mathbf{u}^d - \mathbf{u}^d_{ex}|$.

as $O(h^2)$, as predicted by the error analysis in §3. The uncorrected values for $\mathbf{u}^s$ (blue) are observed to converge as $O(h)$. This is consistent with the results in Table 1 for G_1, in view of the second order root of F_1 at $\mathbf{x} = \mathbf{x}_0$. On the other hand, the leading order terms for $\mathbf{u}^d$, given by the errors in G_2, satisfy $E[\cdot] = O(h/d)$ and are unbounded near the interface. Thus, in the case of $\mathbf{u}^d$, the corrections reduce $O(h/d)$ errors to $O(h^2)$.

Figure 6 plots the errors $|\mathbf{u}^s - \mathbf{u}^s_{ex}|$ and $|\mathbf{u}^d - \mathbf{u}^d_{ex}|$ on a fine grid of target points not on the interface, for the same spherical testcase considered above, but computed with the $O(h^3)$ method. To better distinguish the near-singular errors from the background, for this figure we used the 6th order standard trapezoid rule T_6 instead of T_4. The top frames (a,b,c) show the single layer results, the bottom frames (d,e,f) show the double layer results. The left column (a,d) shows the uncorrected trapezoid values $E_6[G]$, clearly showing large values near the interface. The middle column (b,e) shows the corrected trapezoid values $E_6[G] + E_6[\mathcal{H}] = E^*[G]$. Here, the errors are significantly reduced near the interface, except near the axis. The $O(h^3)$ errors near the interface remain larger than the background errors, which are $O(h^6)$. The right column (c,f) shows the results with the additional correction near the axis $E^*[G] + E^*[B]$. The results near the point $\mathbf{x}_{ax}$ on the axis are much improved, with slightly larger errors remaining in a small ϵ-neighbourhood of $\mathbf{x}_{ax}$, where $\epsilon = \sqrt{h}/4$ for the double layer, and $= h$ for the single layer. In this remaining small region we obtain the velocity components using a 6th order interpolating polynomial based on accurate values on the axis, and accurate values outside of the region. Details are given in Appendix C. The figure shows that the large errors obtained with a standard trapezoid rule near the interface, as seen in column 1, are removed by the corrections.

Figure 7 plots the maximum error obtained after correction with both the $O(h^3)$ and the $O(h^4)$ method. The maximum is taken over the whole domain shown in figure 6 for the $O(h^3)$ method, and over $r > 0.05$ for the $O(h^4)$ method. The maximum errors converge at the predicted rate. For completeness, pointwise error plots similar to figure 6, for both the $O(h^3)$ and the $O(h^4)$ methods using $n = 100, 200, 400, 800$ are included in the supplementary materials to this paper.

The results in this section thus show that in the sample test case the predicted convergence rates for the $O(h^2)$, $O(h^3)$ and $O(h^4)$ methods are attained.

4.2 **The Nozzle**

Next we apply the corrected quadratures to model flow through an axi-symmetric tapered nozzle of length L, with exit radius R_0, and tapering angle β. The nozzle is modelled by an axi-symmetric distribution of Stokeslets on two surfaces, denoted

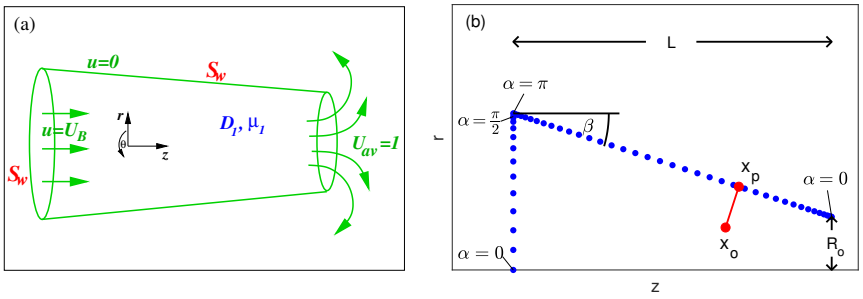

Fig. 8 (a) Sketch of axi-symmetric surfaces modelling a nozzle such that flow is parallel at the back surface, and zero on the lateral surfaces. (b) Discretization of the surfaces in the symmetry plane by gridpoints clustered at the ends of the lateral (or top) surface, and at the top of the back surface.

together by S_w in figure 8(a), that induce the desired flow on S_w: the Stokeslet forces along the flat back piece of S_w induce a prescribed parallel flow; the forces on the lateral surface ensure zero flow at the wall. That is, we choose forces $\mathbf{f}$ that satisfy the equation

$$\mathbf{U}_w(\mathbf{x}_0) = \int_{S_w} M(\mathbf{x}, \mathbf{x}_0) \cdot \mathbf{f}_w \, ds \ , \quad \mathbf{x}_0 \in S_w \tag{4.1}$$

where $\mathbf{U}_w(\mathbf{x}_0) = \langle U, 0 \rangle$ along the back, and $\mathbf{U}_w(\mathbf{x}_0) = 0$ on the lateral piece. To accomodate the incompatibility of the boundary conditions at the top left corner of the nozzle, we leave a gap of size $0.002L$ between the lateral surface and the flat back piece. The surfaces are discretized in the symmetry plane by $n_{top} + n_{back} + 2$ Tschebichev points that cluster at the tips of the back and the top pieces, where the force distribution $\mathbf{f}(s)$, where s is arclength, grows unboundedly. In particular, $\mathbf{f}(s) \sim s^{-1/2}$ as $s \to 0$. The quadratic clustering of the Tchebishev points corresponds to a change of variables $s = L(1-\cos\alpha)/2$ chosen such that, as $s \to 0$, the product $\mathbf{f}(s(\alpha))s_\alpha$ stays bounded, as will be shown in Figure 9 below. The resulting point distribution for $n_{top} = 50$ and $n_{back} = 12$ is shown in figure 8(b).

To find the forces $\mathbf{f}$, we evaluate the singular integral in (4.1),

$$\int_a^b M(\mathbf{x}, \mathbf{x}_0) \cdot \mathbf{f}_w(s(\alpha)) s_\alpha \, d\alpha \tag{4.2}$$

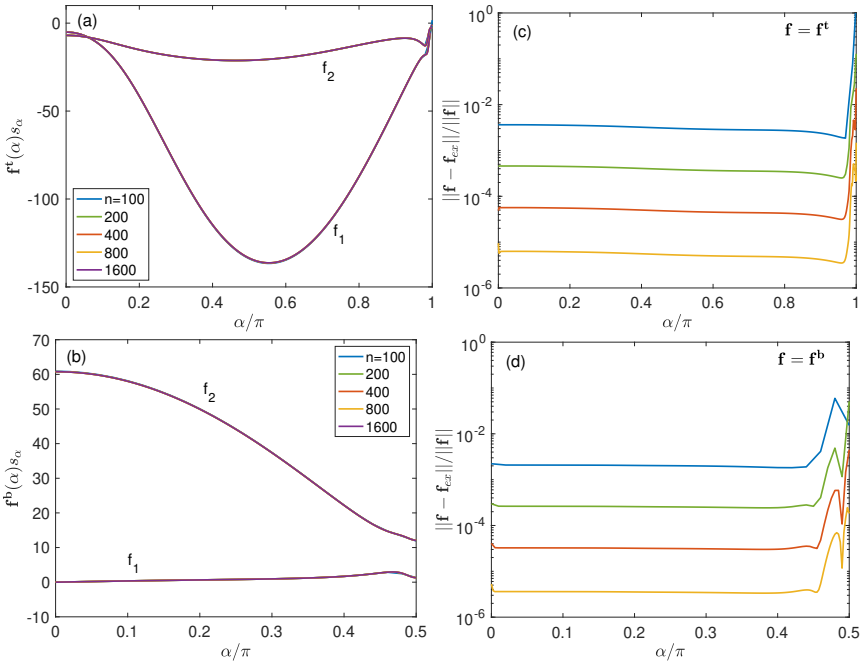

Fig. 9 (a,b) Forces f_1 and f_2 along top (a) and back (b), computed with the indicated values of n. (c,d) Corresponding relative errors $|\mathbf{f} - \mathbf{f_{ex}}|_2/|\mathbf{f_{ex}}|_2$ along top (c) and back (d).

where $\mathbf{x}_0 \in S_w$, using a 3rd order quadrature rule given in [40] (see also [30]). This yields a Fredholm integral equation of the first kind for the forces $\mathbf{f}_j = \mathbf{f}(\alpha_j)$ at the gridpoints. The corresponding matrix A has slightly increasing condition numbers $K(A)$ as $n_{top} + n_{back}$ increases, but for all our computations, $K(a) \leq 4,000$. Figure 9(a,b) shows the resulting forces using our current approach with $n_{top} = 100, 200, 400, 800, 1600$ with corresponding values of $n_{back} = n_{top}/4$. The errors for $n_{top} = 100, 200, 400, 800$, computed by comparing with $n_{top} = 1600$, are shown in figures (c,d). The errors are seen to decay as $O(h^3)$. They are almost constant except near the back top corner. This is caused by the imposed discontinuity in the boundary conditions mentioned above. However, the effect of the discontinuity on the fluid velocity is negligible, as will be seen later, in Figure 11.

To illustrate, figure 10 plots the velocity field induced by the wall forces shown in figure 9. Here, the integral (4.2) is near-singular for points $\mathbf{x}_0$ near the wall and is evaluated, as a function of α, using the method of this paper. Figure 11 plots the errors in the induced velocity field, on a fine grid around the surface S_w. In figure (a), the velocity is computed with the uncorrected trapezoid rule T_4 with $n = 100$. In figures (b-e), the velocity is computed with the corrected $O(h^3)$ method using $n = 100, 200, 400, 800$. The corrections remove the large trapezoid errors near the wall. The corrected errors blend into the background errors, which in this case is $O(h^3)$, in view of the convergence rate of the wall forces. The maximum errors occur near the nozzle opening, where the flow speed is largest, and not near the interface. The largest errors are caused by the large magnitude of the $O(h^3)$ errors in the wall forces and could be reduced using a higher order approximation of the singular integrals.

The maximum errors over the whole domain are plotted in figure 12. The corrected values decay to order $O(h^3)$, while the uncorrected ones decay as $O(h)$, as expected. These results are applied next to simulate the evolution of the double emulsion moving through a nozzle [10].

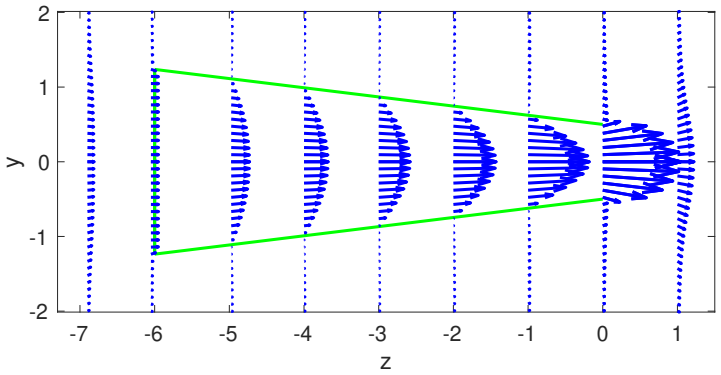

Fig. 10 Velocity field induced by wall forces.

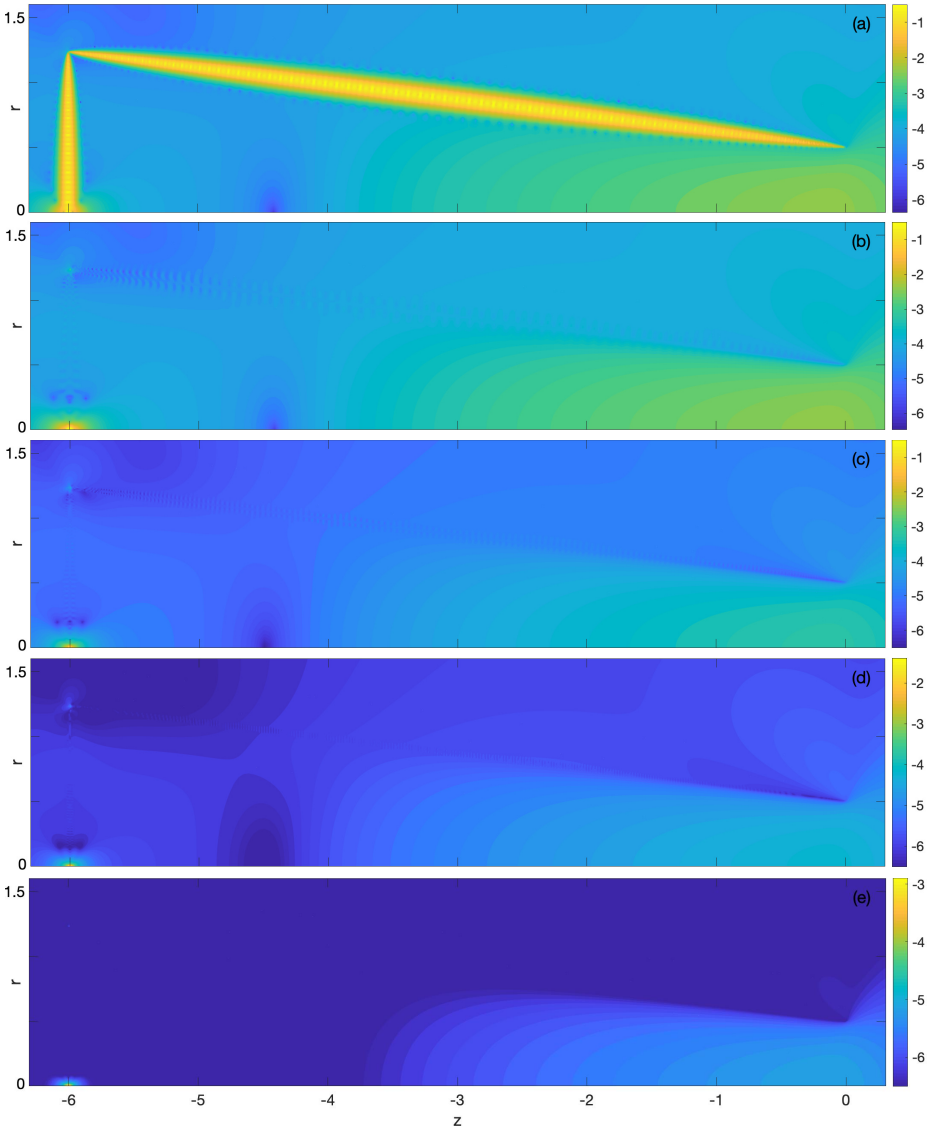

Fig. 11 Errors in velocity induced by wall forces, computed with (a) $n_{top} = 100$, uncorrected (b) $n_{top} = 100$, corrected (c) $n_{top} = 200$, corrected (d) $n_{top} = 400$, corrected (e) $n_{top} = 800$, corrected In each case, $n_{back} = n_{top}/4$.

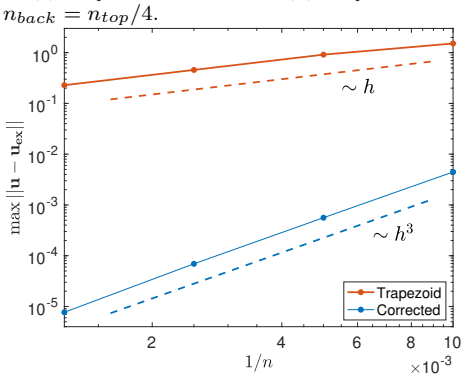

Fig. 12 Maximum errors $\max |\mathbf{u} - \mathbf{u}_{ex}|$ in the velocity induced by the wall forces, vs $1/n = h/\pi$.

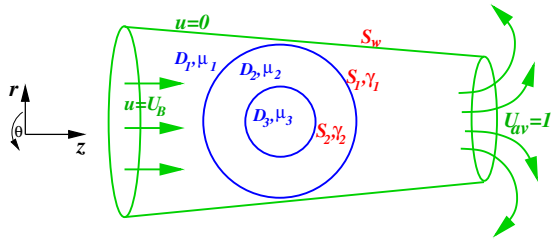

Fig. 13 Sketch of axi-symmetric model for double emulsion flow through nozzle.

4.3 **Double Emulsions motion through nozzle**

The double emulsion flow is modelled by three surfaces, S_1, S_2 and S_w, where S_w represents the nozzle and induces the driving background flow, and S_1, S_2 represent a nested set of drops, as shown in figure 13. The surfaces bound three regions D_1, D_2, D_3 with viscosities μ_1, μ_2, μ_3. The surface tension on S_1 and S_2 is given by $\gamma_{1,2}$. The uniform parallel background flow is chosen below so that the average velocity at the nozzle exit is a prescribed value $U_{av} = U_0$.

For simplicity, we consider the case where all fluid viscosities are equal $\mu_1 = \mu_2 = \mu_3$. The system of equations governing the double emulsion motion in this case is given by

$$\mathbf{U}_w(\mathbf{x}_0) = \mathbf{F}(\mathbf{x}_0; \mathbf{f}_w), \quad \mathbf{x}_0 \in S_w \tag{4.3a}$$
$$\mathbf{u}_1(\mathbf{x}_0) = \mathbf{F}(\mathbf{x}_0; \mathbf{f}_w), \quad \mathbf{x}_0 \in S_1 \tag{4.3b}$$
$$\mathbf{u}_2(\mathbf{x}_0) = \mathbf{F}(\mathbf{x}_0; \mathbf{f}_w), \quad \mathbf{x}_0 \in S_2 \tag{4.3c}$$

where

$$\mathbf{F}(\mathbf{x}_0; \mathbf{f}_w) = \int_{S_w} M(\mathbf{x}, \mathbf{x}_0) \cdot \mathbf{f}_w(\mathbf{x})\, ds_{\mathbf{x}} - \sum_{k=1}^{2} \frac{1}{Ca_k} \int_{S_k} M(\mathbf{x}, \mathbf{x}_0) \cdot \kappa_k(\mathbf{x}) \mathbf{n}_k(\mathbf{x})\, ds_{\mathbf{x}} \tag{4.3d}$$

Here, κ is the mean curvature

$$\kappa = \frac{\dot{r}\ddot{z} - \dot{z}\ddot{r}}{(\dot{r}^2 + \dot{z}^2)^{3/2}} + \frac{\dot{z}}{r\sqrt{\dot{r}^2 + \dot{z}^2}}$$

and $Ca_k = U_0 \mu_k / \gamma_k$. The integrals are singular whenever $\mathbf{x}_0$ lies on the surface of integration and regular or near-singular otherwise. These equations follow from (2.2) and are equivalent to the formulation in [43]. Equation (4.3a) determines the forces $\mathbf{f}_w$ on S_w through a Fredholm integral equation of the first kind, as described above. Given these forces, equations (4.3b,c) determine the drop velocity at a given time. The initial condition is as illustrated in the sketch.

The drop evolution is computed as follows: S_w is discretized as described in §4.2. This determines a linear system for $\mathbf{f}$ at the gridpoints. The linear system

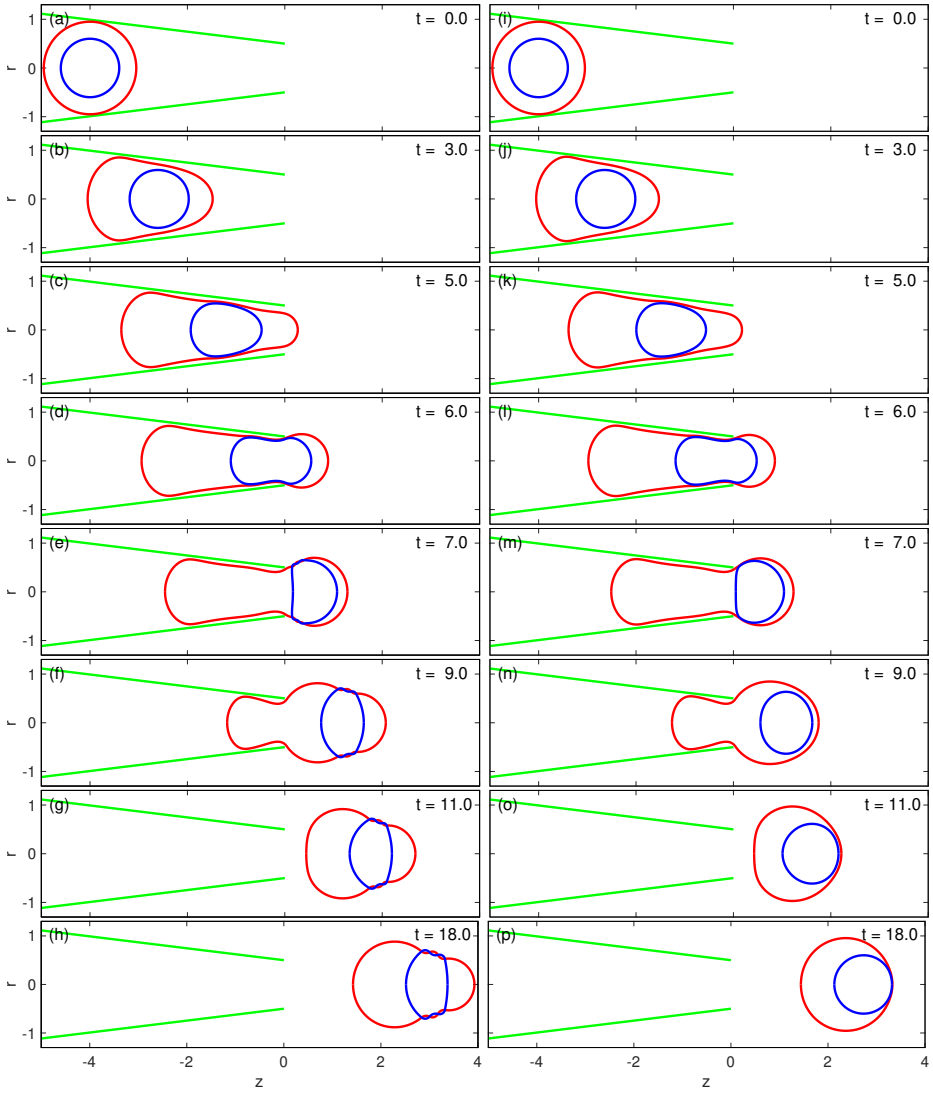

Fig. 14 Evolution of double emulsion droplet in nozzle, at the indicated times. The left column (a-h) uses the uncorrected velocity. The right column (i-p) uses the $O(h^3)$ corrected velocity.

is factored initially so that at each timestep, two triangular solves determine $\mathbf{f}$. The initial surfaces $S_{1,2}$ are discretized using equally spaced points in arclength. Instead of solving for the drop evolution in Cartesian coordinates, we follow [15, 31, 30] and evolve the total arclength L_k and tangent vector angle θ_k for each of the two drops, $k = 1, 2$, in such a way that the discretization points remain equidistant at all times. The resulting system of ordinary differential equations for the arclength and tangent angle are solved using the 4th order Runge Kutta scheme.

Figure 14 shows the solution of these equation at the indicated times. The flow parameters are as follows: the nozzle length indicated in 8(b) is $L = 6$. The angle $\beta = 6^o$. The exit diameter of the nozzle and the average velocity across the opening are $D = 1, U = 1$. Also $Ca_1 = Ca_2 = 0.1$. The drops are initially centered 4 units away from the nozzle with initial radii $R_1 = 0.95$, $R_2 = 0.6$. The figure shows the solution at the indicated times, computed with $n_{top} = 100, n_{back} = 25$, and $n_1 = n_2 = 100$, where $n_{1,2}$ are the number of points on the two drops. The timestep is $\Delta t = 0.005$.

The left column in figure 14 shows the results using the uncorrected 4th order trapezoid rule. The right column shows the results using the corrected $O(h^3)$ quadrature. In the uncorrected results, the two drop interfaces intersect and tangle up around $t = 7$, when they approach each other as they exit the nozzle. Afterwards they remain tangled and do not represent a physical solution. In the corrected results, the drops never tangle up but evolve and approach an apparent steady motion. The closeups in figure 15 show that the corrected results never tangle, nor cross the wall. The results in figure 14 remain unchanged, to the eye, under meshrefinement. To illustrate, results using $n_1 = n_2 = n_{top} = 200$, $n_{back} = 50$, $\Delta t = 0.0025$, as well as $n_1 = n_2 = n_{top} = 400$, $n_{back} = 100$, $\Delta t = 0.00125$, are included in the supplementary materials to this paper.

Three movies are posted as supplementary materials to this paper. The first two show the evolution of the double drops in figures 14 and 15, with and without corrections, both at a large scale and a closeup. The third movie shows the evolution of the example presented in figure 1, with and without corrections. The evolution without corrections breaks down around $t = 7.5$. Similarly, numerical experiments for a range of parameters showed that with the corrected velocity, no tangle occurs and the solution proceeds cleanly to large times, while, with the

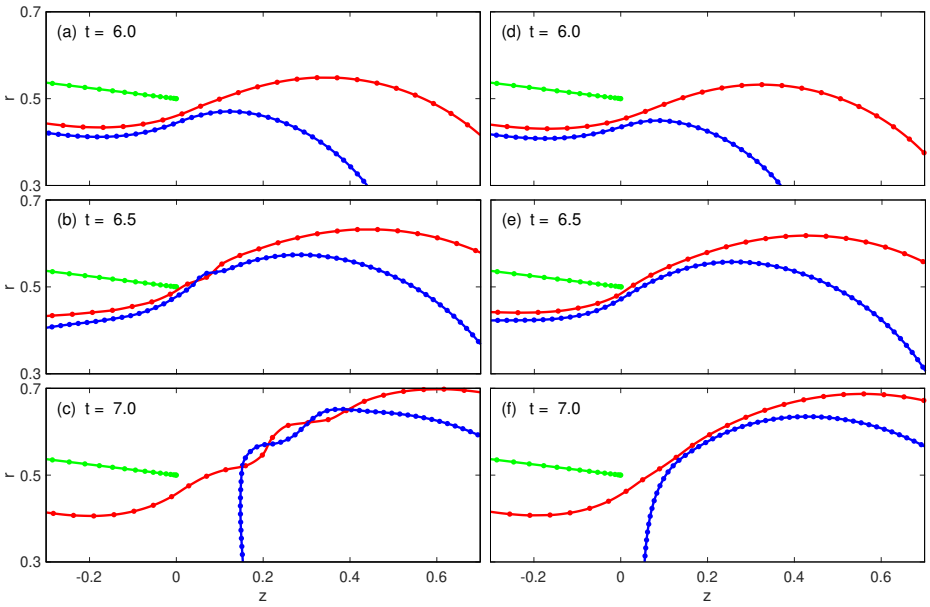

Fig. 15 Closeup of figure 14 at indicated times.

uncorrected velocity, the interfaces intersect and often lead to finite time break up of the solution. These results show that the corrected integration method yields accurate velocities that resolve the flow in an application of interest.

5 Concluding remarks

The paper presents a method to evaluate near-singular integrals in axi-symmetric interfacial Stokes flow. The axi-symmetric boundary integrals are of the form (1.1), where $\mathbf{x}(\alpha)$ is the domain of integration, $\omega(\alpha)$ is a density function, and $\mathbf{x}_0$ is the target point, at a distance d of the interface $\mathbf{x}(\alpha)$. The integrals are near-singular if $0 < d \ll 1$. The method consists of approximating the integrand G for small d by a function $\mathcal{H}$ that captures the near-singularity and is integrated exactly. The remainder $G - \mathcal{H}$ is integrated using any quadrature of choice, where we choose a 4th order trapezoidal rule with uniform meshsize h. In essence, the method consists of adding a correction to the trapezoid approximation of G. The approximation $\mathcal{H}$ is obtained using Taylor series approximations of the interface $\mathbf{x}(\alpha)$ and the density $\omega(\alpha)$ about the orthogonal projection of the target point onto the interface. A following application of the geometric series yields an expansion of $\mathcal{H}$ in terms of basis functions that can be integrated exactly. The order of accuracy depends on the number of basis functions used in the approximation. The paper describes the necessary details to apply the method in axi-symmetric Stokes flow. It applies $O(h^2)$, $O(h^3)$ and $O(h^4)$ versions to test cases and to a sample flow of double droplets moving through a nozzle. The results for the test cases show that the single and double layer potentials are evaluated to within the theoretically predicted accuracy. The results for the double droplet flow show that the problem of tangling of nearby interfaces that occurs with inaccurate integral evaluation is removed after corrected integration.

We conclude with some remarks on the method. (1) The method is conceptually simple, simple to implement, with proven convergence results. (2) It is based on approximations about a base point α_b on the interface, and depends on derivatives of $\mathbf{x}(\alpha)$ and $\omega(\alpha)$ at α_b. An $O(h^m)$ method generally requires m derivatives of $\mathbf{x}$, and $m-1$ derivatives of ω. If the boundary $\mathbf{x}(\alpha)$ consists of a solid surface that does not evolve in time, its derivatives can be found accurately at no cost. In general, the derivatives are obtained to the necessary order of accuracy by interpolating values at the grid point obtained by finite differences. (3) The corrections can be computed using a local set of $2n_{win}$ gridpoints centered at α_b. Thus, for fixed order m the method requires $O(n_{win}N_t)$ operations per timestep, where N_t is the number of nearby target points. Larger values of m require larger values of n_{win} and larger number of basis functions. (4) The application of the geometric series yields, in essence, a generalization of the integrals of analytic functions $1/(z-z_0)^j$ used successfully in planar geometries. It thus lends itself to extensions to surface integrals in fully 3D geometries, which are ultimately the main problem of interest.

In summary, we have addressed the evaluation of near-singular integrals in a geometry not previously considered in the literature, including non-periodic finite interfaces, using a method based on some novel ideas that may contribute to further development.

The code used for the simple spherical test case in §4.1 is publicly available on the Github repository [29], as are all the Mathematica files used to obtain the asymptotic expansions of the integrands G.

Acknowledgments. I thank Anna-Karin Tornberg for hosting me and for many helpful discussions during a short visit at KTH in April 2019.

A The functions Mij, Q_{ijk}

$$
\begin{aligned}
M_{11} &= r(I_{10} + \xi^2 I_{30})/(8\pi) \\
M_{12} &= r\xi(rI_{30} - r_o I_{31})/(8\pi) \\
M_{21} &= r\xi(rI_{31} - r_o I_{30})/(8\pi) \\
M_{22} &= r[I_{11} + (r^2 + r_o^2)I_{31} - rr_o(I_{30} + I_{32})]/(8\pi), \\
Q_{111} &= -6r\xi^3 I_{50}/(8\pi), \\
Q_{112} &= -6r\xi^2(rI_{50} - r_o I_{51})/(8\pi), \\
Q_{122} &= -6r\xi(r_o^2 I_{52} + r^2 I_{50} - 2rr_o I_{51})/(8\pi), \\
Q_{211} &= -6r\xi^2(rI_{51} - r_o I_{50})/(8\pi), \\
Q_{212} &= -6r\xi[(r^2 + r_o^2)I_{51} - rr_o(I_{50} + I_{52})]/(8\pi), \\
Q_{222} &= -6r[r^3 I_{51} - r^2 r_o(I_{50} + 2I_{52}) + rr_o^2(I_{53} + 2I_{51}) - r_o^3 I_{52}]/(8\pi),
\end{aligned}
\tag{A.1}
$$

where $\xi = z - z_0$ and $Q_{121} = Q_{112}, Q_{121} = Q_{212}$ with

$$
\begin{aligned}
I_{10} &= \frac{4}{c} F(k), \\
I_{11} &= \frac{4}{c} a[bF(k) - E(k)], \\
I_{30} &= \frac{4}{c^3} E_{3/2}(k), \\
I_{31} &= \frac{4}{c^3} a[bE_{3/2}(k) - F(k)], \\
I_{32} &= \frac{4}{c^3} a^2[b^2 E_{3/2}(k) - 2bF(k) + E(k)], \\
I_{50} &= \frac{4}{c^5} E_{5/2}(k), \\
I_{51} &= \frac{4}{c^5} a[bE_{5/2}(k) - E_{3/2}(k)], \\
I_{52} &= \frac{4}{c^5} a^2[b^2 E_{5/2}(k) - 2bE_{3/2}(k) + F(k)], \\
I_{53} &= \frac{4}{c^5} a^3[b^3 E_{5/2}(k) - 3b^2 E_{3/2}(k) + 3bF(k) - E(k)],
\end{aligned}
\tag{A.2}
$$

where $\xi = z - z_o$, $k^2 = 4rr_o/(\xi^2 + (r + r_o)^2)$,

$$
E_{3/2} = \frac{E(k)}{1 - k^2} \ , \quad E_{5/2}(k) = \frac{1}{3(1 - k^2)} \left[\frac{2(2 - k^2)}{1 - k^2} E(k) - F(k) \right] \ ,
$$

F and E are the complete elliptic integrals of the first and second kind, respectively:

$$
F(k) = \int_0^{\pi/2} \frac{d\theta}{\sqrt{1 - k^2 \sin^2\theta}} \ , \quad E(k) = \int_0^{\pi/2} \sqrt{1 - k^2 \sin^2\theta} d\theta \ ,
$$

and $a = 2/k^2$, $b = (2 - k^2)/2$, $c^2 = (r + r_o)^2 + \xi^2$. These functions have singularities as $|\mathbf{x} - \mathbf{x}_0|^2 = (r - r_o)^2 + (z - z_0)^2 \to 0$. Using expansions for F, E as $k \to 1$ (see, eg, [1], we find that to leading order in this limit,

$$
\begin{aligned}
I_{1j} &\approx \frac{2}{r_0} \log|\mathbf{x} - \mathbf{x}_0| \ , \\
I_{3j} &\approx \frac{2}{r_0} \frac{1}{|\mathbf{x} - \mathbf{x}_0|^2} + \frac{a_j}{4r_0^3} \log|\mathbf{x} - \mathbf{x}_0| \ , \\
I_{5j} &\approx \frac{4}{3r_0} \frac{1}{|\mathbf{x} - \mathbf{x}_o|^4} + \frac{b_j}{4r_0^3} \frac{1}{|\mathbf{x} - \mathbf{x}_o|^2} + \frac{c_j}{64r_0^5} \log|\mathbf{x} - \mathbf{x}_o| \ ,
\end{aligned}
\tag{A.3}
$$

where $a_0 = 1$, $a_1 = -3$, $a_2 = -7$, $b_0 = 1$, $b_1 = -3$, $b_2 = -7$, $b_3 = -11$, $c_0 = 3$, $c_1 = -5$, $c_2 = 19$, $c_3 = 75$ (obtained with Mathematica). These expressions yield equations (2.4) in §2.2.

B The functions $F(x, x_0)$

The functions $F_j(\mathbf{x}, \mathbf{x}_0)$ defined in Eq (2.4) are listed here, in addition to their to leading order behaviour in $|\mathbf{x} - \mathbf{x}_0|$, as $|\mathbf{x} - \mathbf{x}_0| \to 0$:

$$
\begin{aligned}
F_2^{Q222}(\mathbf{x}, \mathbf{x}_0) &= -\frac{2}{rr_0\rho_2}\left[r^2 - r_0^2 + \xi^2\right]\left[r^2 - r_0^2 - \xi^2\right]^2 && \sim |\mathbf{x} - \mathbf{x}_0|^3 \\
F_1^{Q222}(\mathbf{x}, \mathbf{x}_0) &= -\frac{3}{2rr_0\rho_2^3}\Big[(r - r_0)^2(r + r_0)^3(3r + r_0) \\
&\qquad +(r - r_0)\xi^2(r + r_0)^2(5r + 3r_0) \\
&\qquad -3\xi^4(r^2 + 4rr_0 + 3r_0^2) - 5\xi^6\Big] && \sim |\mathbf{x} - \mathbf{x}_0|^2 \\
F_0^{Q222}(\mathbf{x}, \mathbf{x}_0) &= \frac{3}{16rr_0\rho_2^5}\Big[-(r - r_0)(r + r_0)^3(r^2 + 22rr_0 + 9r_0^2) \\
&\qquad +\xi^2(r + r_0)^2(17r^2 + 46rr_0 + 33r_0^2) \\
&\qquad +3\xi^4(11r^2 + 24rr_0 + 13r_0^2) + 15\xi^6\Big] && \sim |\mathbf{x} - \mathbf{x}_0|^1 \\
F_2^{Q221}(\mathbf{x}, \mathbf{x}_0) &= -\frac{4\xi}{r_0\rho_2}\left[(r^2 - r_0^2)^2 - \xi^4\right] && \sim |\mathbf{x} - \mathbf{x}_0|^3 \\
F_1^{Q221}(\mathbf{x}, \mathbf{x}_0) &= -\frac{3\xi}{r_0\rho_2^3}\left[(r^2 - r_0^2)^2 + 4(r + r_0)^2\xi^2 + 3\xi^4\right] && \sim |\mathbf{x} - \mathbf{x}_0|^3 \\
F_0^{Q221}(\mathbf{x}, \mathbf{x}_0) &= -\frac{3\xi}{8r_0\rho_2^5}\left[(r + r_0)^2(5r^2 + 22rr_0 + 5r_0^2)\right. \\
&\qquad \left.+8(r + r_0)^2\xi^2 + 3\xi^4\right] && \sim |\mathbf{x} - \mathbf{x}_0|^1 \\
F_2^{Q211}(\mathbf{x}, \mathbf{x}_0) &= -\frac{8r\xi^2}{r_0\rho_2}\left[r^2 - r_0^2 + \xi^2\right] && \sim |\mathbf{x} - \mathbf{x}_0|^3 \\
F_1^{Q211}(\mathbf{x}, \mathbf{x}_0) &= \frac{6r\xi^2}{r_0\rho_2^3}\left[r^2 + 4rr_0 + 3r_0^2 + \xi^2\right] && \sim |\mathbf{x} - \mathbf{x}_0|^2 \\
F_0^{Q211}(\mathbf{x}, \mathbf{x}_0) &= -\frac{3r\xi^2}{4r_0\rho_2^5}\left[r^2 + 8rr_0 + 7r_0^2 + \xi^2\right] && \sim |\mathbf{x} - \mathbf{x}_0|^2 \\
F_2^{Q122}(\mathbf{x}, \mathbf{x}_0) &= -\frac{4\xi}{r\rho_2}(r^2 - r_0^2 - \xi^2)^2 && \sim |\mathbf{x} - \mathbf{x}_0|^3 \\
F_1^{Q122}(\mathbf{x}, \mathbf{x}_0) &= -\frac{3\xi}{r\rho_2^3}\Big[(r - r_0)(r + r_0)^2(5r + 3r_0) \\
&\qquad -2\xi^2(r^2 + 4rr_0 + 3r_0^2) - 3\xi^4\Big] && \sim |\mathbf{x} - \mathbf{x}_0|^2 \\
F_0^{Q122}(\mathbf{x}, \mathbf{x}_0) &= \frac{3\xi}{8r\rho_2^5}\left[19r^4 + 48r^3r_0 + 16rr_0(r_0^2 + \xi^2)\right. \\
&\qquad \left.+3(r_0^2 + \xi^2)^2 + 2r^2(21r_0^2 + 5\xi^2)\right] && \sim |\mathbf{x} - \mathbf{x}_0|^1 \\
F_2^{Q121}(\mathbf{x}, \mathbf{x}_0) &= -\frac{8\xi^2}{\rho_2}(r^2 - r_0^2 - \xi^2) && \sim |\mathbf{x} - \mathbf{x}_0|^3 \\
F_1^{Q121}(\mathbf{x}, \mathbf{x}_0) &= -\frac{6\xi^2}{\rho_2^3}\left[3r^2 + 4rr_0 + r_0^2 + \xi^2\right] && \sim |\mathbf{x} - \mathbf{x}_0|^2 \\
F_0^{Q121}(\mathbf{x}, \mathbf{x}_0) &= \frac{3\xi^2}{4\rho_2^5}\left[7r^2 + 8rr_0 + r_0^2 + \xi^2\right] && \sim |\mathbf{x} - \mathbf{x}_0|^2 \\
F_2^{Q111}(\mathbf{x}, \mathbf{x}_0) &= -\frac{16r\xi^3}{\rho_2} && \sim |\mathbf{x} - \mathbf{x}_0|^3 \\
F_1^{Q111}(\mathbf{x}, \mathbf{x}_0) &= -\frac{12r\xi^3}{\rho_2^3} && \sim |\mathbf{x} - \mathbf{x}_0|^3 \\
F_0^{Q111}(\mathbf{x}, \mathbf{x}_0) &= \frac{9r\xi^3}{2\rho_2^5} && \sim |\mathbf{x} - \mathbf{x}_0|^3
\end{aligned}
$$

$$
\begin{aligned}
F_1^{M_{22}}(\mathbf{x},\mathbf{x}_0) &= \frac{1}{r_0\rho_2}\left[(r^2-r_0^2)^2-\xi^4\right] && \sim\ |\mathbf{x}-\mathbf{x}_0|^2\\
F_0^{M_{22}}(\mathbf{x},\mathbf{x}_0) &= -\frac{1}{4r_0\rho_2^3}\left[(r+r_0)^2(5r^2-2rr_0+5r_0^2)\right.\\
&\qquad \left.+4\xi^2(3r^2+4rr_0+3r_0^2)\right] && \sim\ |\mathbf{x}-\mathbf{x}_0|^0\\
&\quad +\frac{|\mathbf{x}-\mathbf{x}_0|^2}{32r_0\rho_2^3}(13r^2+54rr_0+13r_0^2)+O(|\mathbf{x}-\mathbf{x}_0|^4)\\
F_1^{M_{21}}(\mathbf{x},\mathbf{x}_0) &= \frac{2r\xi}{r_0\rho_2}(r^2-r_0^2+\xi^2) && \sim\ |\mathbf{x}-\mathbf{x}_0|^2\\
F_0^{M_{21}}(\mathbf{x},\mathbf{x}_0) &= \frac{r\xi}{2r_0\rho_2^3}(r^2+4rr_0+3r_0^2+\xi^2) && \sim\ |\mathbf{x}-\mathbf{x}_0|^1\\
&\quad +\frac{|\mathbf{x}-\mathbf{x}_0|^2}{\rho_2^3}\frac{\xi}{4}+O(|\mathbf{x}-\mathbf{x}_0|^4)\\
F_1^{M_{12}}(\mathbf{x},\mathbf{x}_0) &= \frac{2\xi}{\rho_2}(r^2-r_0^2-\xi^2) && \sim\ |\mathbf{x}-\mathbf{x}_0|^2\\
F_0^{M_{12}}(\mathbf{x},\mathbf{x}_0) &= -\frac{\xi}{2\rho_2^3}(3r^2+4rr_0+r_0^2+\xi^2) && \sim\ |\mathbf{x}-\mathbf{x}_0|^1\\
&\quad -\frac{|\mathbf{x}-\mathbf{x}_0|^2}{\rho_2^3}\frac{\xi}{4}+O(|\mathbf{x}-\mathbf{x}_0|^4)\\
F_1^{M_{11}}(\mathbf{x},\mathbf{x}_0) &= \frac{4r\xi^2}{\rho_2} && \sim\ |\mathbf{x}-\mathbf{x}_0|^2\\
F_0^{M_{11}}(\mathbf{x},\mathbf{x}_0) &= -\frac{r}{\rho_2^3}(2r^2+4rr_0+2r_0^2+3\xi^2) && \sim\ |\mathbf{x}-\mathbf{x}_0|^0\\
&\quad -\frac{|\mathbf{x}-\mathbf{x}_0|^2}{2\rho_2^3}(r)+O(|\mathbf{x}-\mathbf{x}_0|^4)
\end{aligned}
$$

where $\rho_2^2=(r+r_0)^2+(z-z_0)^2$ and $\xi=z-z_0$. The Mathematica notebooks used to obtained these expansions are posted on Github [29], and a sample pdf posted in the supplementary materials.

C Integrands for $r_0 = 0$. Evaluation for small $r_0 = 0$

If $\mathbf{x}_0$ lies on the axis, with radial component $r_0 = 0$, the expressions for M_{ij}, Q_{ijk} given in Appendix A are not valid. Instead, the limiting expressions of the integrands in (2.3) as $r_0 \to 0$ are found by expanding M and Q about $r_0 = 0$ using known expansions of $F(k)$ and $E(k)$ about $k = 0$. Here we list the resulting expressions, in addition to their 1st and 2nd derivatives in the radial direction at $r_0 = 0$ that are used for interpolation in an $O(h)$ neighbourhood of x_{ax}. Note that the axial velocity components u_s, u_d are even about $r_0 = 0$, while the radial components v_s, v_d are odd. We only list the expressions for the nonzero functions that follow

from this symmetry:

$$
\begin{aligned}
u_s(z_0,0) &= \frac{2\pi}{\mu}\int_a^b \frac{r}{(r^2+\xi^2)^{3/2}}[f_2 r\xi + f_1(2\xi^2+r^2)]\,d\alpha\ ,\\
\frac{\partial v_s}{\partial r_0}(z_0,0) &= \frac{\pi}{\mu}\int_a^b \frac{r}{(r^2+\xi^2)^{5/2}}(f_2 r + f_1\xi)(r^2-2\xi^2)\,d\alpha\ ,\\
\frac{\partial^2 u_s}{\partial r_0^2}(z_0,0) &= \frac{\pi}{\mu}\int_a^b \frac{r}{(r^2+\xi^2)^{7/2}}[3f_2 r\xi(r^2-4\xi^2) + f_1(r^4+8r^2\xi^2-8\xi^4)]\,d\alpha\ ,\\
u_d(z_0,0) &= -12\pi\int_a^b \frac{r\xi}{(r^2+\xi^2)^{5/2}}(vr+u\xi)(r\dot z - \xi\dot r)\,d\alpha\ ,\\
\frac{\partial v_d}{\partial r_0}(z_0,0) &= -6\pi\int_a^b \frac{r}{(r^2+\xi^2)^{7/2}}\Big[\dot z r[vr(r^2-4\xi^2)+u\xi(2r^2-3\xi^2)]\ ,\\
&\qquad\qquad -\dot r\xi[vr(2r^2-3\xi^2)+u\xi(3r^2-2\xi^2)]\Big]\,d\alpha\ ,\\
\frac{\partial^2 u_d}{\partial r_0^2}(z_0,0) &= -6\pi\int_a^b \frac{r\xi}{(r^2+\xi^2)^{9/2}}\Big[\dot z(7r^4 v + 15r^3 u\xi - 26r^2 v\xi^2 - 20ru\xi^3 + 2v\xi^4)\ ,\\
&\qquad\qquad -5\dot r\xi(3r^3 v + 5r^2 u\xi - 4rv\xi^2 - 2u\xi^3)\Big]\,d\alpha\ .
\end{aligned}
\tag{C.1}
$$

where throughout, $\xi = z(\alpha) - z_0$. The derivatives with respect to α of the integrands at the endpoints needed for the trapezoidal rule (3.3b) are computed using finite differences if $\mathbf{x}(a)$ and $\mathbf{x}(b)$ do not lie on the axis, or using exact expressions when they are on the axis, in which case $a = 0$, $b = \pi$. These exact expressions are

$$
\begin{aligned}
&\frac{d}{d\alpha}[G_s^u]_e = \frac{4\pi f_{1,e}\dot r_e}{|\xi_e|},\quad \frac{d}{d\alpha}\Big[\frac{\partial G_s^v}{\partial r_0}\Big]_e = -\frac{2\pi f_{1,e}\dot r_e}{|\xi_e|\xi_e},\quad \frac{d}{d\alpha}\Big[\frac{\partial^2 G_s^u}{\partial^2 r_0}\Big]_e = -\frac{8\pi f_{1,e}\dot r_e}{|\xi_e|\xi_e^2},\\
&\frac{d}{d\alpha}[G_d^u]_e = \frac{12\pi \dot r_e^2 u_e}{\xi_e|\xi_e|},\quad \frac{d}{d\alpha}\Big[\frac{\partial G_d^v}{\partial r_0}\Big]_e = -\frac{12\pi \dot r_e^2 u_e}{\xi_e^2|\xi_e|},\quad \frac{d}{d\alpha}\Big[\frac{\partial^2 G_s^u}{\partial r_0^2}\Big]_e = -\frac{60\pi \dot r_e^2 u_e}{\xi_e^3|\xi_e|}.
\end{aligned}
\tag{C.2}
$$

where subscript e denotes evaluation at the endpoint (either $\alpha = 0$ or $\alpha = \pi$). If $(z_0, 0)$ is near the interface, the integrals (C.1) are near singular and are computed accurately using the corrections described in this paper for $p = 3, 5, 7, 9$.

The velocity and radial derivatives on the axis, given by (C.1), are used to evaluate the single and double layer Stokes potentials for target points in an ϵ-neighbourhood of $\mathbf{x}_{ax}$, where the corrections $E^*[G] + E^*[B]$ lose accuracy, in order to obtain the uniform $O(h^3)$ convergence presented in Figure 7. We obtain velocities in this region using a 6th order polynomial interpolant of the values on the axis and a value on the upper boundary of this region along an arc $r_a(\alpha), z_a(\alpha)$ parallel to the interface.

References

1. Abramowitz, M., (eds), I.A.S.: Handbook of Mathematical Functions: With Formulas, Graphs, and Mathematical Tables,. Dover Publications, New York, (1965)
2. Anna, S.L.: Droplets and bubbles in microfluidic devices. Annu. Rev. Fluid Mech. **48**, 285–309 (2016)
3. Barnett, A., Wu, B., Veerapaneni, S.: Spectrally accurate quadratures for evaluation of layer potentials close to the boundary for the 2d Stokes and Laplace equations. SIAM J. Sci. Comput. **37**(4), 519–542 (2015)
4. Barnett, A.H.: Evaluation of layer potentials close to the boundary for Laplace and Helmholtz problems on analytic planar domains. SIAM J. Sci. Comput. **36**(2), A427–A451 (2014)
5. Beale, J.T., Lai, M.C.: A method for computing nearly singular integrals. SIAM J. Numer. Anal. **38**(6), 1902–1925 (2001)
6. Beale, J.T., Ying, W., Wilson, J.R.: A simple method for computing singular or nearly singular integrals on closed surfaces. Comm. Comput. Phys. **20**, 733–753 (2016)

7. de Bernadinis, B., Moore, D.W.: A ring-vortex representation of an axi-symmetric vortex sheet, in Studies of Vortex Dominated Flows, eds M. Y. Hussaini and M. D. Salas. Springer, New York (1987)
8. Bystricky, L., Palsson, S., Tornberg, A.K.: An accurate integral equation method for stokes flow with piecewise smooth boundaries. Bit Numer Math **61**, 309–335 (2021)
9. Carvalho, C., Khatri, S., Kim, A.D.: Asymptotic analysis for close evaluation of layer potentials. J. Comp. Phys. **355**, 327–341 (2018)
10. Chen, H., Li, J., Shum, H.C., Stone, H.A., Weitz, D.A.: Breakup of double emulsions in constrictions. Soft Matter **7**, 2345–2347 (2011)
11. Cortez, R.: The method of regularized Stokeslets. SIAM J. Sci. Comput. **23**(4), 1204–1225 (2001)
12. Epstein, C.L., Greengard, L., Klöckner, A.: On the convergence of local expansions of layer potentials. SIAM J. Numer. Anal. **51**(5), 2660–2679 (2013)
13. Guo, H., Zhu, H., Liu, R., Bonnet, M., Veerapaneni, S.: Optimal slip velocities of micro-swimmers with arbitrary axisymmetric shapes. J. Fluid Mech. **910** (2021)
14. Helsing, J., Ojala, R.: On the evaluation of layer potentials close to their sources. J. Comp. Phys. **227**, 2899–2921 (2008)
15. Hou, T., Lowengrub, J., Shelley, M.: Removing the stiffness from interfacial flows with surface tension. J. Comp. Phys. **114**, 312–338 (1994)
16. Jensen, M.J., Stone, H.A., Bruus, H.: A numerical study of two-phase Stokes flow in an axisymmetric flow-focusing device. Phys. Fluids **18**, 077103–285 (2006)
17. Khatri, S., Kim, A.D., Cortez, R., Carvalho, C.: Close evaluation of layer potentials in three dimensions. J. Comp. Phys. **423**, 109798 (2020)
18. Klinteberg, L.a., Tornberg, A.K.: A fast integral equation method for solid particles in viscous flow using quadrature by expansion. J. Comp. Phys. **326**, 420–445 (2016)
19. Klinteberg, L.a., Tornberg, A.K.: Error estimation for quadrature by expansion in layer potential evaluation. Adv. Comput. Math. **43**, 195–234 (2017)
20. Klinteberg, L.a., Tornberg, A.K.: Adaptive quadrature by expansion for layer potential evaluation in two dimensions. SIAM J. Sci. Comp. **40**(3), A1225–A1249 (2018)
21. Klöckner, A., Barnett, A., Greengard, L., O'Neil, M.: Quadrature by expansion: A new method for the evaluation of layer potentials. J. Comp. Phys. **252**, 332–349 (2013)
22. Ladyzhenskaya, O.A.: The boundary value problems of mathematical physics,. Springer-Verlag (2010)
23. Lee, S.H., Leal, L.G.: The motion of a sphere in the presence of a deformable interface. II. A numerical study of a translation of a sphere normal to an interface. J. Colloid Interface **87**, 81–106 (1982)
24. Marin, O., Runborg, O., Tornberg, A.K.: Corrected trapezoidal rules for a class of singular functions. IMA J. Numer. Anal. **34**(4), 1509–1540 (2014)
25. Nie, Q., Baker, G.: Application of adaptive quadratrue to axi-symmetric vortex sheet motion. J. Comp. Phys **143**, 49–69 (1998)
26. Nitsche, M.: Axisymmetric vortex sheet motion: accurate evaluation of the principal value integrals. SIAM J. Sci. Comput. **21**(3), 1066–1084 (1999)
27. Nitsche, M.: Singularity formation in a cylindrical and a spherical vortex sheet. J. Comput Phys. **173**(1), 208–230 (2001)
28. Nitsche, M.: Evaluation of near-singular integrals with application to vortex sheet flow. Theoretical and Computational Fluid Dynamics pp. doi:10.1007/s00162–021–00577–9 (2021)
29. Nitsche, M.: Axisymmetric stokes flow - near singular integrals. https://github.com/monikanitsche/axistokes-nearsing (2022)
30. Nitsche, M., Ceniceros, H.D., Karniala, A.L., Naderi, S.: High order quadratures for the evaluation of interfacial velocities in axi-symmetric Stokes flows. J. Comp. Phys. **229**, 6318–6342 (2010)
31. Nitsche, M., Steen, P.H.: Numerical simulations of inviscid capillary pinchoff. J. Comp. Phys. **200**, 299–324 (2004)
32. Ojala, R., Tornberg, A.K.: An accurate integral equation method for simulating multi-phase Stokes flow. J. Comp. Phys. **298**, 145–160 (2015)
33. Palsson, S., Siegel, M., Tornberg, A.K.: Simulation and validation of surfactant-laden drops in two-dimensional stokes flow. J Comp Phys **386**, 218–247 (2019)
34. Pérez-Arancibia, C., Faria, L.M., Turc, C.: Harmonic density interpolation methods for high-order evaluation of Laplace layer potentials in 2D and 3D. Journal of Computational Physics **376**, 411–434 (2019)

35. Pozrikidis, C.: Boundary integral and singularity methods for linearized viscous flow. Cambridge University Press, Cambridge (1992)
36. Pozrikidis, C.: Interfacial dynamics for Stokes flow. J. Comput Phys. **69**, 250–301 (2001)
37. Quaife, B., Biros, G.: High-volume fraction simulations of two-dimensional vesicle suspensions. J Comp Phys **274**(1), 245–267 (2014)
38. Rahimian, A., Barnett, A., Zorin, D.: Ubiquitous evaluation of layer potentials using quadrature by kernel-independent expansion. BIT Numerical Mathematics **58**(2), 423–456 (2018)
39. Sidi, A.: Application of a class of $\mathscr{I}_m$ variable transformations to numerical integration over surfaces of spheres. J Comput. Appl. Math. **184**, 475–492 (2005)
40. Sidi, A., Israeli, M.: Quadrature methods for periodic singular and weakly singular Fredholm integral equations. J Sci. Comput. **3**(2), 201–231 (1988)
41. Siegel, M., Tornberg, A.K.: A local target specific quadrature by expansion method for evaluation of layer potentials in 3d. J. Comp. Phys. **364**, 365–392 (2018)
42. Stone, H.A., Duprat, C.: Low-Reynolds-Number Flows, in Fluid-Structure Interactions in Low-Reynolds-Number Flows, eds Camille Duprat Howard Stone. Royal Society of Chemistry (2012)
43. Stone, H.A., Leal, L.G.: Breakup of concentric double emulsion droplets in linear flows. J. Fluid Dyn. **211**, 123–156 (1990)
44. Tlupova, S., Beale, J.T.: Nearly singular integrals in 3d Stokes flow. Comm. Comput Phys. **14**, 1207–1227 (2013)
45. Tlupova, S., Beale, J.T.: Regularized single and double layer integrals in 3d Stokes flow. J. Comp. Phys. **386**, 568–584 (2019)
46. Wu, B., Martinsson, P.G.: Corrected trapezoidal rules for boundary integrals in three dimensions. Arxiv (2021)
47. Wu, B., Martinsson, P.G.: Zeta correction: a new approach to constructing corrected trapezoidal quadrature rules for singular integral operators. Adv. Comput. Math. **47**(45) (2021)
48. Ying, L., Biros, G., Zorin, D.: A high-order 3d boundary integral equation solver for elliptic pdes in smooth domains. J Comp Phys **219**(1), 247–275 (2006)